Imaging atoms and molecules on surfaces by scanning tunnelling microscopy

2011 J. Phys. D: Appl. Phys. 44 464001

(http://iopscience.iop.org/0022-3727/44/46/464001)

IOP Publishing Journal of Physics D: Applied Physics
J. Phys. D: Appl. Phys. **44** (2011) 464001 (19pp) doi:10.1088/0022-3727/44/46/464001

Imaging atoms and molecules on surfaces by scanning tunnelling microscopy

Shirley Chiang

Department of Physics, University of California Davis, 1 Shields Avenue, Davis, CA 95616-8677, USA

Received 29 July 2011
Published 4 November 2011
Online at stacks.iop.org/JPhysD/44/464001

Abstract
This review discusses nearly 30 years of scanning tunnelling microscopy (STM) work on high resolution imaging of numerous materials systems, giving a historical perspective on the field through the author's work. After a brief discussion of early STM and atomic force microscope (AFM) instrumentation development, the review discusses high resolution STM imaging on semiconductors, metals on semiconductors, Au(1 1 1), metal on metals including surface alloys, oxygen on metals, molecules adsorbed on metals, and AFM measurements of friction on graphite and mica.

(Some figures in this article are in colour only in the electronic version)

1. Introduction

School children used to learn, 'You can't see atoms'. The scanning tunnelling microscope (STM), however, changed that when it was invented 30 years ago by Gerd Binnig and Heinrich Rohrer at the IBM Zurich Research Laboratory [1–4]. Based on the principle of quantum mechanical tunnelling between two electrical conductors, a sharp tip and a solid surface, the STM has revolutionized our ability to measure surfaces down to the atomic level. Binnig and Rohrer won half of the 1986 Nobel Prize in Physics for the development of the STM. The Nobel Press Release said, 'It is evident that this technique is one of exceptional promise, and that we have so far seen only the beginning or its development' [5]. In the intervening 25 years, we have seen the technique applied to all sorts of materials systems, from metals to semiconductors to superconductors, in environments from vacuum to gas to solution, and with applications to materials, catalysis, chemical reactions and biology. Not only can one routinely 'see' atoms on a surface using the STM, but commercial instruments are reliable and commonly found in every surface science laboratory. Indeed, the STM has indeed fulfilled its prophecy of 'exceptional promise'.

Most surface structures had previously been determined by low energy electron diffraction (LEED), which measures the two-dimensional Fourier transform of the atomic structure. Detailed structure determinations involve multiple scattering calculations to fit experimental data (consisting of LEED I–V curves) to careful structural models [6]. For the first time, the STM allowed the measurement of direct real space images of surfaces, together with steps and defects. Interpretation of images can still be difficult, however, due to the fact that the STM really measures the electronic structure of the surface, rather than the surface topography. In addition, the structure of the tip is also involved in the tunnelling process. Nevertheless, a simple perturbation theory approach indicated that the STM can be considered to measure the local density of states of the surface (LDOS) at the position of the tip [7, 8]. For metal surfaces, often the bumps observed in an STM image can be interpreted as individual atoms [9]. For semiconductors, typically the situation is complicated by dangling bonds and the polarity of bias voltage, as the STM can measure either filled or empty states of the sample. For example, when measuring GaAs, the STM image shows the positions of Ga atoms when using positive sample bias to measure unoccupied sample states, but it shows the As atoms when using negative sample bias to measure occupied states [10]. For molecules on metals, typically the STM measures the molecular orbitals of the molecule hybridized with the metal electronic states [11].

In 1986, Gerd Binnig, Calvin Quate and Christoph Gerber invented the atomic force microscope (AFM), which allowed measurements of small forces and of the topography of insulating surfaces [12]. In their original instrument, they placed a diamond tip on the end of a lever near a surface and used an STM to measure the deflection of the lever, which was proportional to the force between the tip and surface. This instrument has found applications from industry to biology.

I first heard about the STM when I had a telephone conversation with the hiring manager, Eric Kay, at the IBM San Jose Research Laboratory (which later became the IBM

Almaden Research Center). Fortunately, I heard Heini Rohrer's invited talk at the American Physical Society meeting in March 1983 before I went to my job interview. I was amazed to hear his descriptions of the instrument and to see his pictures of individual atoms on surface, especially the real space images of the mysterious Si(1 1 1) 7 × 7 reconstruction [13]. I finished writing my PhD dissertation, got married, and visited the IBM Zurich Research Laboratory briefly while on my honeymoon in Europe. I returned to California in October 1983 to start my new job at IBM San Jose to build an ultrahigh vacuum (UHV) STM, in collaboration with Robert Wilson, who had also been hired that same year. I will give a personal account of my experiences building first an STM and later an atomic force microscope. This review gives a personal view of nearly thirty years of STM research, explaining results from a variety of materials systems. Most of the work described comes from our group, obtained during a time when almost everything we measured with our STM and AFM gave surprising new and exciting results. Our work in the first decade after the invention of the STM demonstrated atomic and molecular imaging on semiconductors, metals on semiconductors, metals, metal epitaxial growth, surface metal alloying, atomic adsorbates on metals, molecules on metals, calculations of predicted STM images of molecules, and measurement of surface frictional forces by AFM. In addition, I will describe some recent work on related materials systems.

2. Instrumentation development

We developed two unique instruments at IBM Almaden: (1) an UHV STM with interchangeable samples and tips, connected to a surface analysis system [14] and (2) an AFM which used an optical interference technique to measure the lever deflection [15]. The design philosophies of both instruments are described in more detail below.

2.1. UHV STM

When we began to design our STM, we had several design constraints: (1) we wanted to use thin-walled piezoelectric tubes for the scanner, so that high voltage operational amplifiers, with ±150 V power supplies, could be used for the output stage of our electronic feedback loop and still allow enough motion from the scanner elements. (2) We wanted to be able to interchange the tips without breaking vacuum. (3) We wanted to control the microscope and acquire the data with a computer. (4) We wanted to connect the UHV chamber for the STM to a commercial surface analysis system so that we could examine the sample with other techniques without breaking vacuum.

The schematic diagram of our successful STM design is shown in figure 1 [14]. The tripod scanner consisted of three piezoelectric tubes, 3.17 mm outer diameter, 25.4 mm long, with 0.5 mm wall thickness, with sensitivity of ~100 Å V^{-1} giving a working range of 3 μm with our homemade analogue electronic feedback loop. An interchangeable tip for our system was simply a piece of wire bent to have a hook at one end, so that a wobble stick with a solid wire on the end could be used to remove it from the STM. Since we exchanged only the tip wire itself, the mounting block to hold it in the STM could have very low mass and could be easily moved using the piezoelectric tubes. The louse walker in this STM had a 3 mm thick piezoelectric body and anodized aluminium feet, similar to that of the 'pocket-size' STM developed at IBM Zurich by Christoph Gerber and co-workers [16].

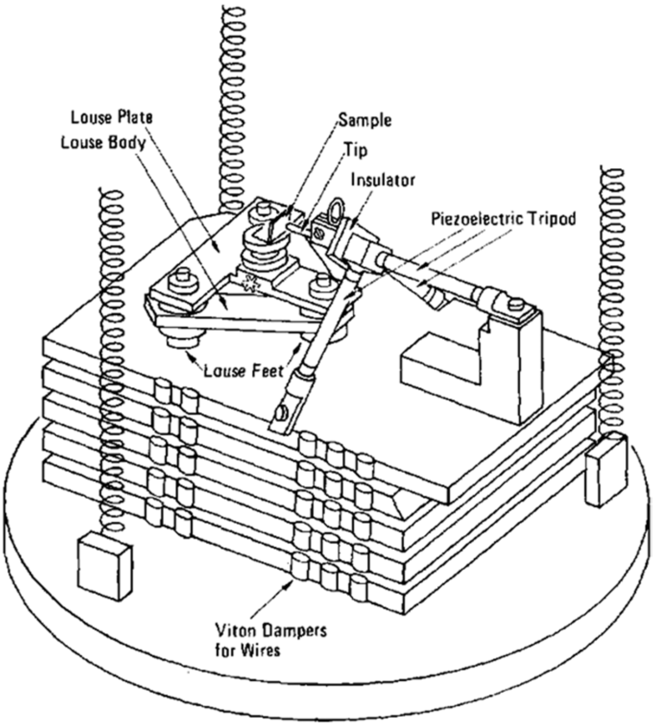

Figure 1. Schematic diagram of UHV STM, showing pocket STM hung on double-spring stages. The louse piezoelectric walker carrying the sample is on the left, and the piezoelectric tube tripod for scanning the tip is shown on the right. Reprinted with permission from [14]. Copyright 1988 American Vacuum Society.

This STM combined two common methods of vibration isolation. Its principal components were mounted onto a stack of stainless-steel plates separated by Viton rubber, like the 'pocket' STM [16]. This stack was then mounted onto a set of double spring stages with magnet eddy current damping, with the magnets and copper blocks tilted at 45° from the vertical to improve the damping in both vertical and horizontal planes. Since the STM chamber was quite tall, by moving the STM itself to the bottom level, we were able to make the two spring stages linear, making the balancing much easier.

The STM was controlled with an IBM PC/XT. The data acquisition program was written in C, with the inner loop written in 8086 assembly language to obtain sufficient speed. Real-time display of the scan lines was observed on both a storage oscilloscope and the computer display, and the computer was used to generate top-view colour STM images.

This STM was connected by a transfer chamber with a rotatable rack and pinion mechanism to a VG Escalab Mark II. The surface analysis system was equipped with 500 Å resolution scanning Auger microscopy/scanning electron microscopy (SAM/SEM), a dual-anode Al/Mg x-ray source for x-ray photoemission spectroscopy (XPS), and an argon ion gun

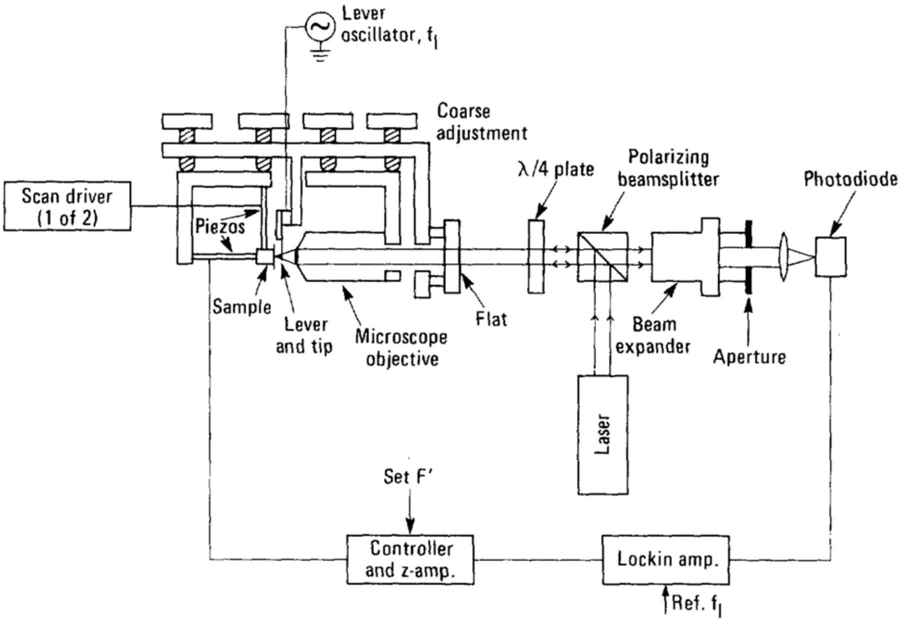

Figure 2. Schematic diagram of AFM using optical interferometry to detect lever deflection. Reprinted with permission from [15]. Copyright 1988 American Vacuum Society.

for depth profiling and ion scattering spectroscopy (ISS). The sample preparation chamber contained an airlock, an electron beam sample heater, a high-energy argon ion sputtering gun, rear view LEED optics, and an evaporator for deposition of sub-monolayer metal films onto the sample surfaces. The transfer chamber not only connected the Escalab to the dedicated STM chamber with its own large ion pump, but its rotating mechanism also permitted other subsidiary chambers to be easily connected to the vacuum system.

The STM tips were usually made from 0.5 mm tungsten wire, which was bent into the appropriate shape and then etched in KOH with either ac or dc voltage like field emission tips [17]. The SEM capability of the Escalab allowed measurements of the shapes and sizes of tips formed using different procedures [18].

At UC Davis, we later completed the construction of an STM with *in situ* tip and sample exchange, which operated at 85 K to study molecules on surfaces [19]; this instrument has recently been rebuilt [20].

2.2. AFM using optical interferometry

Shortly after the AFM was invented by Binnig, Quate and Gerber at Stanford [12], Gary McClelland and I decided to work together with two postdoctoral fellows, Ragnar Erlandson from Sweden and Mathew Mate, to build one at our lab. We decided that we did not want to use an STM to detect the lever deflection, as operating one tip-to-sample junction for the force measurement seemed difficult enough, without having a second tunnelling junction in the instrument as well. We did some quick computations and decided that optical interferometry should have enough sensitivity for the measurements.

The schematic diagram of our AFM using optical interferometry is shown in figure 2 [15]. The sample was mounted onto a tripod scanner made from piezoelectric tubes, similar to that in the STM described above. The lever was made from a tungsten wire with a 90° bend near one end to serve as the AFM tip. It was mounted onto an additional piezoelectric tube which could be used to modulate tip position. A microscope objective lens focused light onto the tip. Both the piezoelectric tripod and the microscope objective could be independently moved with respect to the tip, using systems of 3 fine screws in a kinematic arrangement. The optical interferometer, shown in figure 2, consisted of a HeNe laser, a polarizing beam splitter, a quarter wave plate, an optical flat, a beam expander, an aperture, a lens, and a photodiode. The AFM was supported on a system of plates separated by Viton rubber [16], and the entire optical system was mounted to an aluminium block suspended from four latex tubes. A Plexiglas box isolated the optical path from air currents and acted as an acoustical shield.

At UC Davis, David Muzzall, Don Futaba and I later developed a UHV instrument which could function as both an AFM (using piezoresistive cantilevers) and an STM, with *in situ* tip and sample replacement, and operating at temperatures between 20 K and 400 K [21, 22]; this instrument has recently been rebuilt [23].

3. Semiconductors and metals on semiconductors

3.1. Si(1 1 1) 7 × 7

The famous 3D view of the Si(1 1 1) 7 × 7 surface published by Binnig and Rohrer (figure 3(*a*)) [13] is a photograph of a relief model made by cutting the paper of the original *x*–*y* recorder traces and gluing pieces of cardboard between them; I saw the model at IBM Zurich, and Binnig and Rohrer describe it in their Nobel Lecture [24]. The solution to the puzzle of the atomic arrangement of this surface was finally given

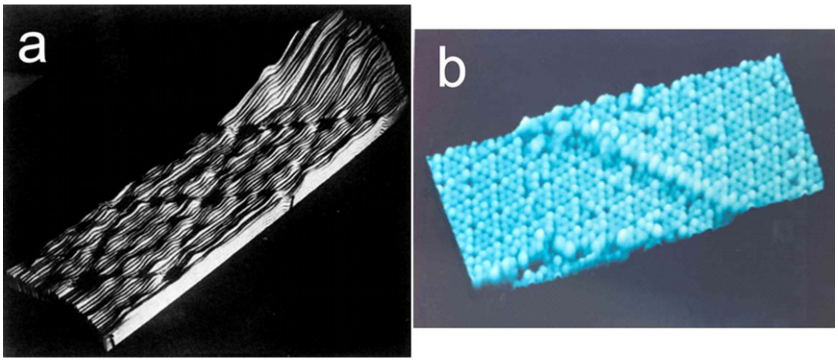

Figure 3. (*a*) STM relief image of two unit cells Si(1 1 1) 7 × 7, measured at 300 °C. Reprinted with permission from [13]. Copyright 1983 American Physical Society. (*b*) Three-dimensional view of the reconstruction of the clean Si(1 1 1) 7 × 7 surface across an atomic step, showing the characteristic 12 adatoms per unit cell and a corrugation of 2 Å. Image processing techniques have been used to enhance the observation of the adatoms on the terraces bordering the step in this ∼290 Å × 170 Å image of filled states of the sample. Reprinted with permission from [27]. Copyright 1987 American Chemical Society.

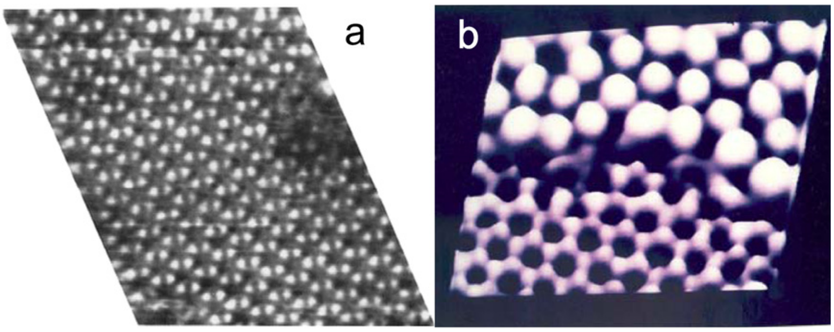

Figure 4. (*a*) STM image of Ag/Si(1 1 1) $(\sqrt{3} \times \sqrt{3})$R30° surface, showing honeycomb arrangement of bright features. Image size 90 Å × 90 Å, corrugation of ordered area ∼1 Å, tip bias $V_T = -0.39$ V. Reprinted with permission from [29]. Copyright 1987 American Physical Society. (*b*) 3D view of STM image of Si(1 1 1) 7 × 7 region (top) next to region of $(\sqrt{3} \times \sqrt{3})$R30° Ag/Si(1 1 1), $V_T = -2.0$ V, $i_T = 2.0$ nA. Reprinted with permission from [27]. Copyright 1987 American Chemical Society.

by Takayanagi in his dimer–adatom–stacking fault (DAS) model, which was determined from transmission electron diffraction and is completely consistent with the real-space STM data [25, 26].

Because the Si(1 1 1) surface is easy to clean by heating alone, and the surface unit cell of the 7 × 7 reconstruction is quite large (25 Å × 50 Å), with a large corrugation of 2 Å, we used it to test the performance of our new STM. Since we measured our data directly with a computer, we could easily process it afterwards to display a 3D image. One of our early images of the Si(1 1 1) 7 × 7 reconstruction, showing a step on the surface, is shown in figure 3(*b*) [27].

3.2. *Ag/Si(1 1 1)* $(\sqrt{3} \times \sqrt{3})$*R30°*

The first system we chose to study with our new STM was the atomic structure of Ag adsorbed on Si(1 1 1), because the system had been studied by many other techniques, and Ag does not diffuse into the bulk [28]. We observed a honeycomb lattice for the $(\sqrt{3} \times \sqrt{3})$R30° surface (figure 4(*a*)), and we also saw rows of atoms on the lower coverage 1 × 3 surface [29]. Directly following our paper in Physical Review Letters was the paper by Van Loenen, Demuth, Tromp, and Hamers from IBM T.J. Watson Research Center in New York [30]. Although the data in both papers were very similar, we suggested that the bright spots in the honeycomb arrangement were Ag atoms, and Van Loenen *et al* used tunnelling spectroscopy and a counting argument about the semiconducting nature of the surface to suggest that the same features must be Si atoms. This started a minor controversy, so that other people began to perform additional experiments. We also continued to do additional experiments ourselves, and we measured some images which showed regions of the Si(1 1 1) 7 × 7 reconstruction immediately adjacent to the Ag/Si(1 1 1) $\sqrt{3}$ structure (figure 4(*b*)). We learned to do image processing on our data in order to enhance the visibility of small features, and we developed the technique of registering the bright spots of the STM image with a known lattice [31]. We then published a second paper on the registration of the bright spots in the $\sqrt{3}$ structure with the Si(1 1 1) lattice, thereby demonstrating that the protrusions were located at three fold hollow sites and were thus consistent with being Ag atoms in the honeycomb structure but not with Si atoms in an embedded trimer structure [32].

The now-accepted model from x-ray diffraction data would have each protrusion in the STM image correspond to 3 Ag atoms, with Ag in the top layer and no Si atoms (i.e. missing top layer) [33–35]. More recent STM measurements performed at 62 K show images with a centred hexagonal arrangement of protrusions, rather than a honeycomb [36].

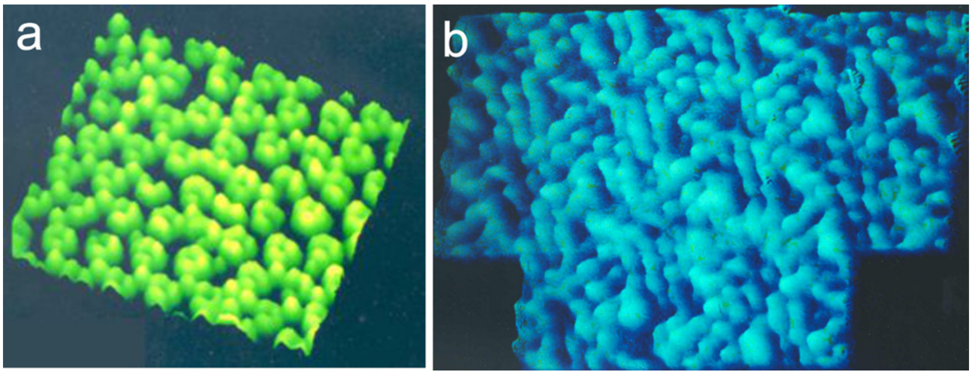

Figure 5. (*a*) STM image of Ni/Si(1 1 1) in the $(\sqrt{19} \times \sqrt{19})$R23.4°structure, $V_T = +1.20$ V, $i_T = 0.2$ nA. 3D view of data from [45]. (*b*) 3D view of STM image of Cu/Si(1 1 1) 5 × 5, ∼120 Å × 80 Å, full scale corrugation ∼ 0.3 Å, $V_T = +0.5$ V, $i_T = 2.0$ nA. 3D view of data from [50].

Density functional theory (DFT) has been used to suggest an inequivalent triangle model (IET) [37]. Recent STM data show inequivalent protrusions in the honeycomb arrangement at room temperature, which would also be consistent with the IET model [38].

Thus, simple interpretations of STM can be difficult, because the STM measures electronic structure and not surface topography. This can, however, be turned into an advantage for studying electronic properties of surfaces. Feenstra and his colleagues found that the surface density of states corresponds to $(dI/dV)/(I/V)$, and they applied this to studies of the cleaved Si(1 1 1) 2 × 1 reconstructed surface [39, 40], spectroscopy of GaAs [41], the structure of oxygen adsorbed on GaAs [42], and the voltage dependence of STM images on semiconductors [43]. Hamers and Demuth pioneered current imaging tunnelling spectroscopy (CITS), which involved measurements of the I–V curve at every point of the raster scan while maintaining an approximately constant sample–tip separation [44]. They first applied this technique to elucidate the electronic structure of the Si(1 1 1) 7 × 7 surface.

3.3. Ni/Si(1 1 1) $(\sqrt{19} \times \sqrt{19})$*R23.4°*

We also studied the structure of Ni adsorbed on Si(1 1 1) at low coverage in the $(\sqrt{19} \times \sqrt{19})$R23.4° structure (figure 5(*a*)) [45]. We therefore interpreted the bumps in the Ni/Si(1 1 1) image as individual Si atoms surrounding Ni atoms at the corners of the unit cell. Parikh, Lee and Bennett used Auger spectroscopy, reflection high energy electron diffraction (RHEED) and STM to show that Ni coverage is 0.15 ML and that there are three Ni atoms per unit cell [46]. Kinoda and Ogawa prepared the $\sqrt{19}$ surface by melting small particles Ni onto the Si(1 1 1) surface; they observed twinned atomic structures and made another atomic model [47].

3.4. Cu/Si(1 1 1) 5 × 5

Frank Salvan from Marseille, France, came to work with us on STM measurements of the Cu/Si(1 1 1) 5 × 5 structure. LEED and Auger electron diffraction observations of non-integral order spots between those expected for 5 × 5 and 6 × 6 structures suggested that this surface was incommensurate with the substrate [48, 49]. Our STM observations of Cu on Si(1 1 1) showed unit cells which were much less well-ordered than those for the Ag/Si(1 1 1) or Ni/Si(1 1 1) surfaces. The surface has 5 × 5 subunits, which pack at spacings varying from 5 to 7 lattice constants. A 3D view of an STM image of filled states on this surface is shown in figure 5(*b*) [50]. Demuth and co-workers also measured STM topographs and CITS images on this surface and made a more detailed model for this quasiperiodic structure [51]. More recent STM studies and models of this surface have also been published [52, 53].

Recently, we have been again studying metals on semiconductors, but now we are studying the interaction of metals with Ge substrates and finding surprising types of growth using low energy electron microscopy (LEEM), together with STM. Pb/Ge(1 1 1) exhibits spontaneous domain switching during phase separation [54]. We have also observed phase coexistence of the $(\sqrt{3} \times \sqrt{3})$R30° and 1 × 1 phases for Pb on Ge(1 1 1) [55]. In addition, we have been studying Ag/Ge(1 1 1), Au/Ge(1 1 1) [56], Ag/Ge(1 1 0) 1D island growth, and Ir/Ge(1 1 1) island growth [57].

4. Au(1 1 1)

4.1. Observation of close-packed atoms

Vickie Hallmark began working with us, and she was interested in finding a flat substrate for studies of molecules. She decided to grow thin films of Au on mica, which grow epitaxially in the (1 1 1) orientation when the mica substrate is held at elevated temperature during growth [58]. When she first tried to measure one of these films in a small STM which we had been operating in air, she found a beautiful hexagonal arrangement of the atoms when she measured the image directly in the variation of the tunnelling current, with the tip scanning approximately a fixed distance from the surface (figure 6(*a*)) [9]. Upon checking the lateral calibration of the instrument carefully, we determined that each of these bumps in the current image corresponded to a close-packed atom of the Au(1 1 1) surface. This was very surprising because, up to that time, the STM had only been used to observe reconstructions with larger atomic spacing, such as the Si(1 1 1) 7 × 7 [13], missing rows on the reconstructed surface of Au(1 1 0) [59], and the 5 × 1 reconstruction of Au(1 0 0) [60]. Therefore,

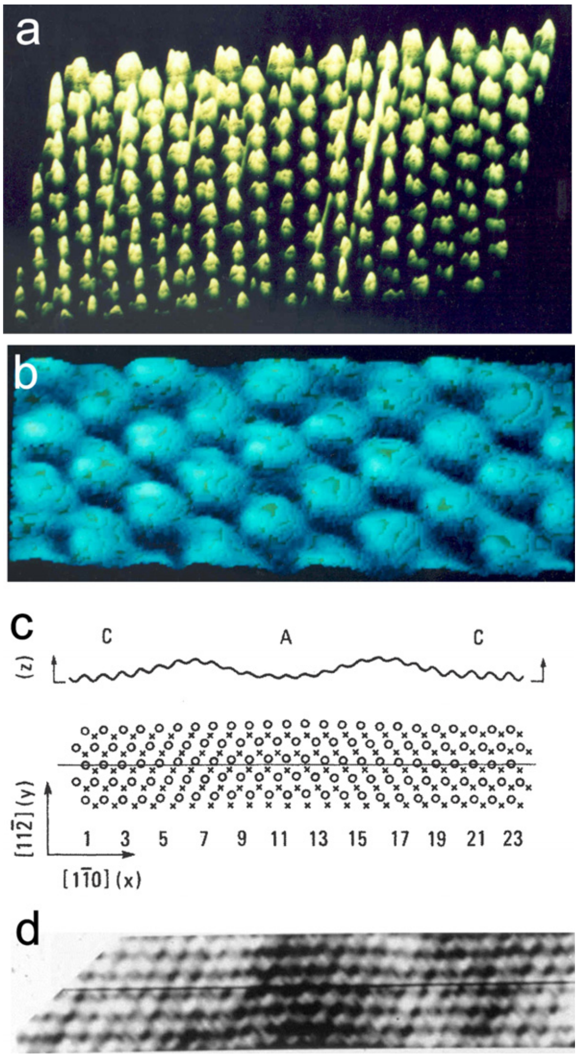

Figure 6. (*a*) STM tunnelling current image of $\sim$25 Å $\times$ 25 Å region of Au(1 1 1) thin film on mica measured in air, with atomic spacing of 2.8 $\pm$ 0.3 Å. The current modulation is $\sim$ 10% with dc level of 2 nA. $V_T = 50$ mV. 3D view of data from [9]. (*b*) Constant current topographical image of Au(1 1 1) thin film on mica measured in UHV. Atomic spacing is 3.0 $\pm$ 0.3 Å, $V_T = 30$ mV, $i_T = 3$ nA. 3D view of data from [9]. (*c*) Model for reconstruction of the Au(1 1 1) surface [61]. The crosses denote the positions of atoms in the second layer, and the open circles denote the positions of atoms in the reconstructed top layer. C and A mark the regions of ABC (fcc) and ABA (hcp) stacking, respectively. The lattice defect at the boundary between the two regions corresponds to a bulk Shockley partial dislocation with Burgers vector $\frac{1}{6}(1,\ 1,\ -2)$. The displacement of the atoms from the straight line which has been drawn in the [1 $\bar{1}$ 0] direction is clear. From [62]. (*d*) Atomic resolution STM image of reconstructed epitaxially grown Au(1 1 1) thin film on mica, measured in UHV. Region of 100 Å $\times$ 40 Å, $V_T = 0.611$ V, $i_T = 0.3$ nA. The atomic resolution of the image allows the determination of the positions of single atoms, and the displacement of the atoms from the straight line in the [1 $\bar{1}$ 0] direction can be directly compared with the model in (*c*). (*c*) and (*d*) reprinted with permission from [62]. Copyright 1989 American Physical Society.

we checked this measurement in our UHV STM operating in constant current mode, and indeed we still saw the individual atoms, with a corrugation amplitude of $\approx$0.3 Å at a tip bias of +30 mV and a tunnelling current of 3 nA (figure 6(*b*)) [9].

4.2. *Au(1 1 1)* $23 \times \sqrt{3}$

Christof Wöll joined our group as a postdoctoral fellow, and he had previously studied the Au(1 1 1) reconstruction with He atom scattering [61]. Their model suggested that the $23 \times \sqrt{3}$ reconstruction is distinguished by regions of fcc stacking separated from regions of hcp stacking by regions in which first layer atoms are in bridge sites between 2 second layer atoms (figure 6(*c*)). Since he even borrowed a Au(1 1 1) single crystal from Toennies' group, we put it into our UHV STM and proceeded to measure the surface reconstruction [62]. Since the atoms in bridge sites are higher, the surface topography in the unit cell shows two parallel ridges, which are pairs of partial dislocations. The top row of atoms are not in a straight line, as seen clearly in figure 6(*d*), since going across the unit cell, they go from fcc to bridge to hcp to bridge and back to fcc sites. We were initially so focused on the atomic structure of the reconstruction that we did not look at larger scale images for a while.

When we did examine the Au(1 1 1) surface in larger images, we discovered the longer range herringbone structure of the reconstruction, where the pairs of partial dislocations apparently alter direction in a fairly regular manner to relieve the surface stress (figure 7) [63]. A more detailed study of the Au(1 1 1) herringbone structure was presented by Barth and coworkers [64]. The system of Cu on Ru(0 0 0 1) shows the same type of pairs of misfit dislocations and has been interpreted with the same model as that for the reconstructed Au(1 1 1) surface [65]. My colleagues, Chambliss and Wilson, also studied the growth of Ag on Au(1 1 1) and discovered finger-like Ag protrusions growing from the step edges. Their data were consistent with a model of diffusion-limited aggregation with local relaxation [63].

Around this time, around the corridor from us, Don Eigler did his tour de force experiment in writing 'IBM' in xenon atoms on a Ni(1 1 0) surface using an STM at 4 K. He picked up individual atoms with the STM tip, moved them over the surface, and then dropped them at a predetermined location on the surface [66]. Jon Mamin then discovered that he could deposit 150–200 Å mounds of Au onto a Au surface from a gold STM tip by applying voltage pulses. In air, he could make mounds on the surface with nearly 100% probability if the amplitude of the voltage pulses exceeded a certain threshold. Repeated pulses could also erase mounds. He created a simplified map of the world with a diameter $\sim 1\ \mu$m. When we tried the same procedure in UHV, we were able to deposit Au mounds but found that the process was significantly less reliable, with perhaps 50% probability of writing. The mounds were also significantly larger than those made in air [67].

5. Metals on metals, including surface alloys

5.1. *Ni/Au(1 1 1)*

When David Chambliss deposited Ni onto our Au(1 1 1) crystal, he found that the Ni islands grew in ordered arrays (figure 8(*a*)) because they nucleated at the 'elbows' of misfit dislocations in the Au(1 1 1) herringbone reconstruction (figures 8(*b*) and (*c*)) [68, 69]. The surface lattice dislocations

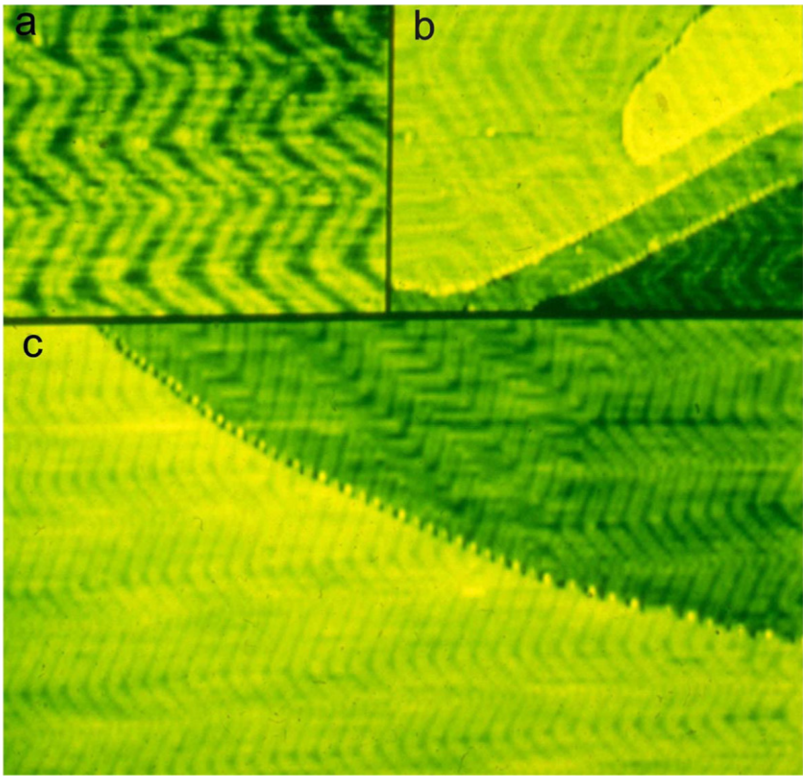

Figure 7. STM images of Au(1 1 1) reconstruction showing 'herringbone' arrangement of partial dislocations on large terraces. The Au(1 1 1) step height, 2.35 Å, was subtracted from terraces in all images where the reconstruction is visible. Dots along the steps are artefacts of the image compression. (*a*) Herringbone pattern on one terrace. Image width 540 Å sample bias $V_S = -2.0$ V. (*b*) Four terraces with uniaxial reconstruction. Image width 740 Å $V_S = 1.2$ V. (*c*) Two terraces with herringbone 'hyperdomains.' Image width 3000 Å, $V_S = -1.0$ V. Reprinted with permission from [63]. Copyright 1991 American Vacuum Society.

at the elbows presumably result in additional chemical reactivity in those regions, causing the Ni islands to nucleate there. Because the herringbone reconstruction has an ordered structure, the Ni islands form an ordered array, with spacing of 73 Å along the $[1\,\bar{2}\,1]$ direction in rows 140 Å apart. When the underlying reconstruction changes direction, the arrangement of the Ni islands does also. Fe on Au(1 1 1) also nucleates at these elbows, although the first layer Fe islands are more triangular, whereas the Ni islands tend to be more hexagonal [70, 71].

5.2. Au/Cu(1 0 0)

Palmberg and Rhodin had observed a $c(2 \times 2)$ LEED pattern for 1/2 ML of Au adsorbed onto Cu(1 0 0) and postulated that the atomic arrangement was that of a CuAu surface alloy corresponding to the (1 0 0) face of the Cu_3Au bulk alloy [72]. Our high resolution STM image of this surface showed $c(2 \times 2)$ ordering with two unequal peaks per unit cell (figure 9(*a*)) [73]. Every other atom of this surface is Cu or Au, with the taller atoms presumably being Au, since Au has a larger atomic radius, and dynamical LEED analysis suggested that the Au atoms are outwardly displaced by 0.01 nm [74]. Figure 9(*a*) also shows narrow, nearly regular buckled ridges along the close-packed [0 1 1] and $[0\,1\,\bar{1}]$ directions, presumably corresponding to regions where these 'nanometre faults' relieve the stress mismatch between the Cu(1 0 0) substrate lattice and the CuAu alloy layer.

The step and island structure of the alloy surface is shown in figure 9(*b*) [73]. After Au deposition, the steps, which are 0.18 nm high, have a zigzag appearance consisting mainly of close-packed [0 1 1] and $[0\,1\,\bar{1}]$ step segments. Islands, which are typically 5 nm wide, appear mainly at the centres of wide terraces and have close-packed edges favouring the same directions. The top layer of the islands has the same $c(2 \times 2)$ surface alloy structure and nanometre faults as the surrounding terrace layer. Therefore, the islands must not only have the same CuAu top layer but also the same pure copper second layer. Presumably alloy formation on the terraces releases Cu atoms which aggregate into the islands when they combine with additional Au deposited on the surface.

5.3. Au/Ag(1 1 0)

We read with interest the reports by Fenter and Gustafsson (FG) that their medium energy ion scattering (MEIS) data indicated that Au grows in bilayers on bilayer on Ag(1 1 0) [75, 76]. This seemed like a surprising new growth mode, which would be easy to observe with STM. After postdoctoral fellow Sylvie Rousset joined us from France, she found that her STM images of this system showed no bilayer growth for Au coverage up to 2.5 ML [77]. For $\leqslant 1$ ML of deposited Au, she observed only monoatomic steps and no islands. The clean Ag(1 1 0) surface showed 'frizzy' monoatomic steps, presumably arising from fluctuations of atomic positions near the step edges, which were

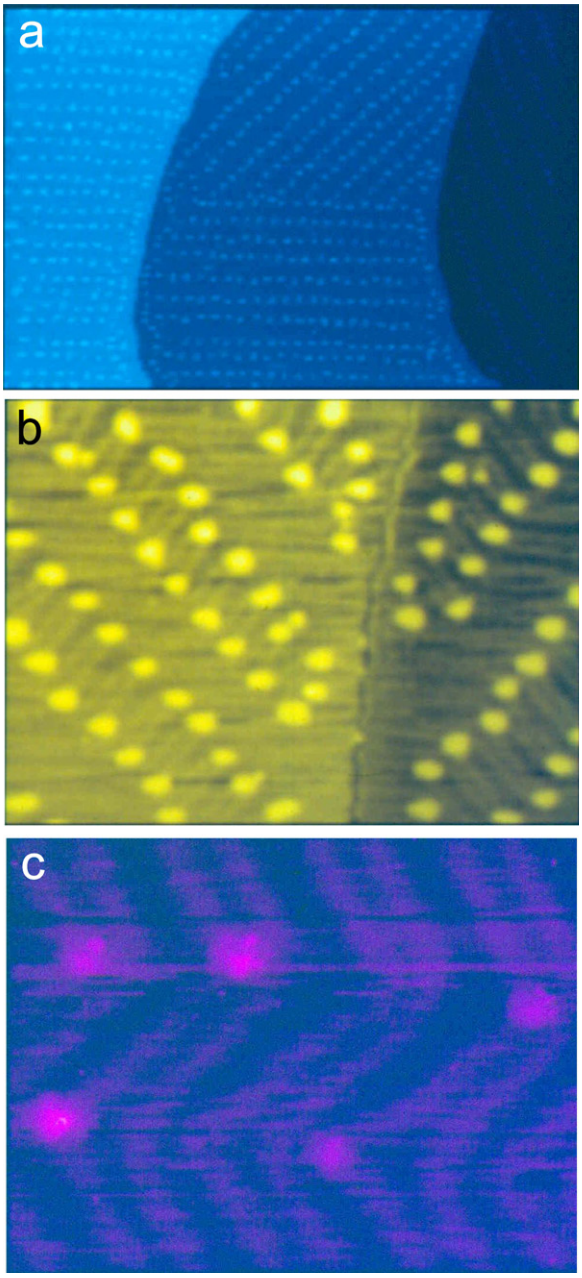

Figure 8. STM images of Ni islands growing at partial dislocations of Au(1 1 1) herringbone structure. (*a*) 0.11 ML Ni on Au(1 1 1), 2900 Å × 2500 Å. Several atomically flat Au terraces are seen, separated by steps of single-atom height. Small light dots on each terrace are monolayer Ni islands, in rows along [1$\bar{2}$1] direction. Island shapes are not resolved here because their size is comparable to the pixel size $(10\,\text{Å})^2$. $V_S = 2.0$ V. (*b*) 0.14 ML Ni on Au(1 1 1), 900 Å × 650 Å. Ni islands nucleate in regular array at elbows of Au herringbone reconstruction. (*c*) 0.01 ML Ni on Au(1 1 1) 280 Å × 250 Å. Clusters of 10 to 12 atoms nucleate at kinks in surface partial dislocations. (*a*) and (*c*) reprinted with permission from [69]. Copyright 1991 American Vacuum Society.

considerably stabilized by 0.3 ML of Au, leading to [1 $\bar{1}$ 0] facets along the step edges. For higher coverage, correlated 2D finger growth began at the steps and then grew into 3D islands, which extended across monoatomic steps, with an elongated shape along the close-packed [1 $\bar{1}$ 0] direction (figure 10(*a*)) [77–79].

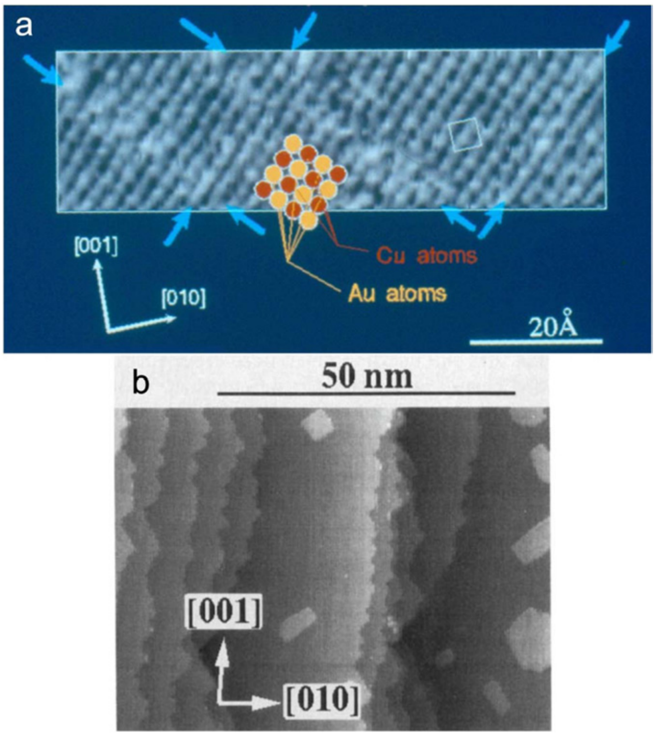

Figure 9. STM images of Au on Cu(1 0 0) $c(2 \times 2)$ alloy structure. (*a*) Atomic resolution image, resolving lattice with both Cu and Au atoms. Alloy structure is indicated by superimposed array of circles, as indicated. Small white square marks a single $c(2 \times 2)$ unit cell, $(0.36\,\text{nm})^2$, with one higher atom (presumably Au) at the centre. Arrows mark regions of disrupted atomic positions associated with ‘nanometre faults’ along [0 1 $\bar{1}$]. $V_s = 0.5$ V. (*b*) Image showing step and island structure. (*b*) reprinted with permission from [73]. Copyright 1992 Elsevier.

David Fowler, who was setting up an MEIS apparatus at IBM Almaden, helped us to re-interpret the published MEIS data [75, 76], together with the STM data [77]. The MEIS data showed a ‘blocking dip curve,’ indicating that deposited Au atoms are shadowed for Au coverage $\geqslant 0.06$ ML, which was evidence for bilayer growth if there were no surface alloying or intermixing of Au and Ag. In addition, the Ag yield decreased linearly with increasing Au coverage up to ∼1 ML, which had previously been interpreted as evidence for lack of intermixing. Since the Ag(1 1 0) surface is quite open, however, two layers of Ag are exposed to the incident He atoms in the MEIS experiment, and thus an Au atom in either the first or second layer could cause the decrease in the Ag yield. Therefore, a model with Au going into the second layer, interchanging with the Ag atoms, is consistent with both the MEIS data and the STM data. We then made a quantitative fit to the MEIS blocking curve and found that the best fit occurred if all of the Au atoms were located below the top Ag layer [77, 78].

From the STM data, we could directly measure the area of atomic layers at different heights in an image showing 2D finger growth with 1.4 ML Au (figure 10(*b*) and (*c*)). After the first monolayer of intermixed Au growing beneath the top Ag layer, both the STM data and the MEIS fits were consistent with additional Au growing on top of the surface in 3D islands. Figure 10(*d*) shows our ‘intermixed Stranski–Krastanov’ growth model for this system. First-principles

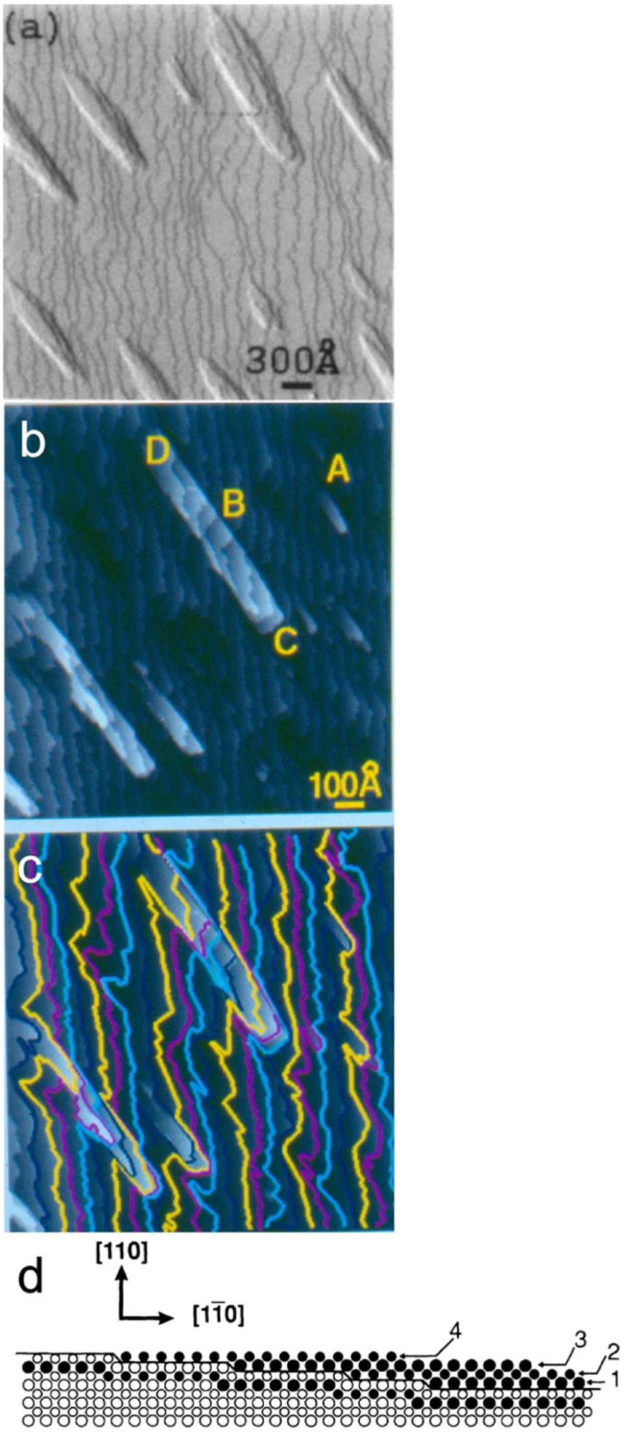

Figure 10. (*a*) Differentiated STM image of 1.8 ML of Au on Ag(11) shows 3D islands growing along $[1\,\bar{1}\,0]$ across monoatomic steps. (*b*) STM image of 1.4 ML Au on Ag(1 1 0) shows transition in growth from 2D fingers to 3D islands. (A) is a biatomic step. (B) indicates multilayer growth. Bottom edge of finger, (C), is multiatomic step perpendicular to $[1\,\bar{1}\,0]$. Top edge of finger, (D), grows from adjacent terrace. (*c*) Same image with lines of constant height drawn along step edges. (*d*) Schematic diagram of 'intermixed Stranski–Kranstanov' growth mode of Au/Ag(1 1 0). Solid (open) circles indicate Au (Ag) atoms. Two circle sizes denote atoms in different vertical (0 0 1) planes. Lines shows step positions after intermixed layer is complete but before fingers grow. For clarity, steps are drawn more closely spaced than in actual sample. Reprinted with permission from [77]. Copyright 1992 American Physical Society.

total-energy calculations also suggested that bilayer growth was energetically unfavourable, and that the most favourable growth mode up to 1 ML coverage energetically would have Au atoms substituting for the Ag atoms in the second layer [80, 81]. Molecular dynamics simulations also suggest intermixing of Au and Ag, with Au going into the second layer, particularly for low Au coverage [82–84]. A later STM study of Au deposited at room temperature showed both island growth and hole formation simultaneously occurring on the surface, and the hole formation was associated with Au atoms burrowing beneath the Ag surface [85].

5.4. Fe/Cu(1 0 0)

Postdoctoral fellow Kevin Johnson measured STM images for Fe on Cu(1 0 0) [86, 87]. At low coverage, the Fe grows epitaxially in the fcc structure of the Cu substrate. Our results showed, however, that for low coverage, the Fe forms inclusions in the Cu surface, causing copper atoms to be ejected and form islands on the surface.(figure 11(*e*)) Subsequently, two or more layers grow simultaneously. See the model described in figures 11(*a*)–(*d*). Additional support for the model comes from quantitative measurement of the areas of the STM image belonging to specific surface layers. The adsorption of oxygen onto the Fe/Cu(1 0 0) allows the identification of the Cu areas versus the Fe ones, as the FeO regions show atomic scale corrugation, whereas the Cu ones appear flat (figure 11(*f*)).

When additional Fe is deposited onto the surface, forming a thick film, the Fe undergoes the martensitic fcc–bcc transition for coverage near 14 ML [88]. Figures 11(*g*) and (*h*) show the identification of fcc and bcc steps from their height. The bcc (1 1 0) grains are highly elongated along the $\langle 0\,1\,1\rangle_{\mathrm{fcc}} \parallel [1\,\bar{1}\,1]_{\mathrm{bcc}}$ direction, with steps along $[0\,0\,1]_{\mathrm{bcc}}$. The STM images show the behaviour of steps at grain boundaries and the presence of tilted surfaces arising from fcc–bcc interfaces.

5.5. Ag-Co/Ru(0 0 0 1)

Graduate student Gayle Thayer used STM to study the relationship between surface stress and the alloy structure of Ag–Co alloys grown on Ru(0 0 0 1) [89, 90]. She found that the CoAg alloy phase had a composition of $Co_{0.6}Ag_{0.4}$ and consisted of droplets of Ag surrounded by Co. For Ag composition above 40%, phase separation occurred, and the additional Ag formed a pure phase which had Ag dislocations. See figure 12(*a*) for an STM image of an 80% Ag film. The phase separation was attributed to the competition between two stress relief mechanisms: surface alloying and dislocation formation [89].

An atomically resolved STM image of the surface alloy is shown in figure 12(*b*). In this image, dark patches of atoms are Ag and are surrounded by brighter Co atoms. The Co atoms adjacent to Ag droplets appear to be brighter. Figure 12(*c*) shows that the brighter Co atoms, i.e. those adjacent to Ag drops, are displaced (in the direction away from those Ag drops) from the hcp sites represented by the hexagonal array of dots in the overlay. The STM images were used to find the atomic displacements at the boundaries between regions

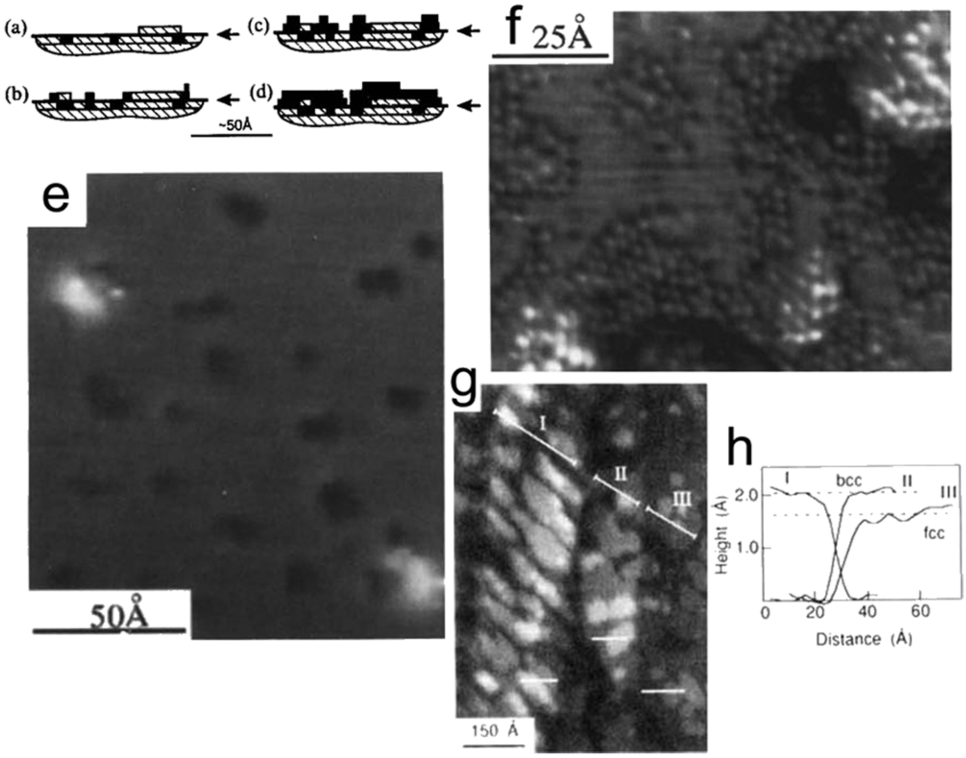

Figure 11. Fe on Cu(1 0 0), with Fe inclusions at very low coverage. (*a*)–(*d*) Schematic representation of surface cross section after room temperature deposition. Solid represents Fe and hatched regions Cu. Arrows denote initial location of (1 0 0) substrate surface. (*a*) At 0.05 ML, deposited Fe exists principally in substrate inclusion. Layer 1 (L1) islands are Cu. (*b*) 0.3 ML Fe adds to edges of islands and nucleates new islands. (*c*) 1.0 ML. Simultaneous growth in first two epitaxial layers. (*d*) 2.0 ML First two layers nearly complete; L3 growth has begun. (*e*) 0.05 ML Fe on Cu(1 0 0), with Fe inclusions as dark spots, and Cu islands as white spots. (*f*) L1 heterogeneity revealed by O_2 decoration. 0.92 ML Fe on Cu(1 0 0) dosed with 2×10^{-6} Torr O_2 causes corrugation of ∼0.4 Å on FeO. Core of ejected substrate Cu atoms does not show the strong corrugation visible at the perimeter, which is mostly Fe. Brighter features are second layer Fe atoms. $V_S = 50$ mV, $I_T = 1.0$ nA. (*g*) 14 ML Fe/Cu(1 0 0), with fcc and bcc steps. (*h*) Plot showing heights of steps in (*g*). (*a*)–(*f*) reprinted with permission from [86]. Copyright 1994 Elsevier. (*g*)–(*h*) reprinted with permission from [88]. Copyright 1993 American Physical Society.

of Co and Ag. The STM image in figure 12(*b*) was used to create an initial alloy configuration for a Frenkel–Kontorova (FK) model with local spin density approximation (LSDA) parameters. After relaxation of this original conformation within the FK model, the image in figure 12(*d*) was computed, with brightness proportional to displacement squared, (Δr^2). This computed image looks very much like the actual data in figure 12(*b*). The FK model was quantitatively compared with parameters extracted from the STM images and could then be used to quantify the energy balance between stress relaxation and chemical bonding in the formation of these surface alloy structures [90].

6. Oxygen on metals

6.1. O/Cu(1 0 0)

We also studied the adsorption of oxygen on Cu(1 0 0), another model surface system which had been extensively studied previously [91]. Our STM images showed two rotational domains with paired atomic rows for a surface exhibiting the $(2\sqrt{2} \times \sqrt{2})R45°$ LEED pattern [92]. The observed atomic corrugation was small, only 0.2 Å. The STM images agreed well with the missing row model determined from the LEED multiple scattering analysis presented in the same paper [92].

6.2. O/W(1 1 0)

Oxygen adsorbed on W(1 1 0) is a model surface system with three ordered phases with increasing coverage, which had been characterized by LEED: (2×1) for 0.5 ML, (2×2) for 0.75 ML and 1×1 for 1.0 ML [93–95]. The LEED analyses placed the oxygen in a triply coordinated site, and there are two such possible sites on the bcc surface. Postdoctoral fellow Kevin Johnson observed all of these oxygen structures and also confirmed this triply coordinated site, with observations of adjacent domains where the oxygen occupied either one of these sites or the other [96]. A region with two such adjacent domains for the 1×1 phase is shown in figure 13(*a*). Note that, due to electronic effects, oxygen is imaged as a depression by the STM [97–99]. The atomic structure of the domain walls, which can be either light or heavy, indicating the amount of oxygen, is shown in the inverted images in figures 13(*b*) and (*c*). After annealing the 1×1 surface to 1250 K, the superstructure shown in figure 13(*d*) is observed, with regularly spaced parallel domain walls along the $[\bar{1}\,1\,3]$ direction. Because of the occurrence of the site-exchanged domains, the width of the domain walls alternates. These ordered domain walls presumably cause the superstructure diffraction features which had previously been attributed to a compressed misfit overlayer [95, 100].

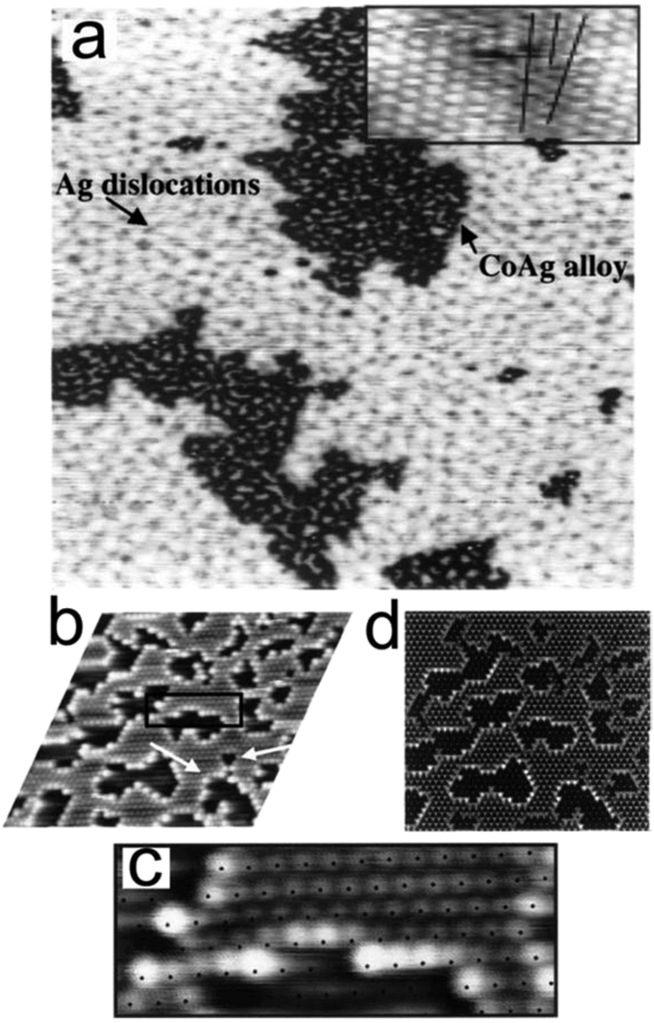

Figure 12. Phase segregation of Co–Ag alloy film, which consists of Ag drops surrounded by Co, on Ru(0 0 0 1) for 80% Ag. The pure Ag phase has a misfit dislocation structure. Inset shows atomic resolution of a single dislocation in the pure Ag phase, with missing row of atoms in the atomic lattice. 1000 Å × 1000 Å, $V_S = 0.58$ V, $I_T = 0.5$ nA. (*b*) Atomically resolved image of CoAg/Ru(0 0 0 1) alloy film. Co atoms at Ag boundaries are imaged substantially brighter than other Co atoms in the figure. Arrows point to two Ag droplets, with Co atoms around the large droplet being noticeably brighter than those around the small droplet. (*c*) The hexagonal array of black dots overlaid on a portion of the image in (*b*) represents hcp sites of the substrate. Co atoms that are imaged bright are clearly displaced form hcp sites while darker Co atoms are not. (*d*) FK model simulation of the CoAg surface alloy. The greyscale of Co atoms bordering Ag droplets in the simulation is keyed to displacement squared, $(\Delta r)^2$. (*a*) reprinted with permission from [89]. Copyright 2001 American Physical Society. (*b*)–(*d*) reprinted with permission from [90]. Copyright 2002 American Physical Society.

More recently, graduate student David Muzzall studied the adsorbate structures and the coverage dependence of oxygen on W(1 1 0) as a function of the deposition pressure for room temperature exposures. He found that the oxygen deposition pressure, and not just the total exposure in Langmuirs, was an important variable in determining the surface structure. For the same total exposure of oxygen, changes in deposition pressure of a factor of 3 caused significant changes in the apparent structures, domain sizes, and the actual resulting coverages of the adsorbate layer. For both the 2 × 1 and 2 × 2 structures, a critical dosing pressure exists, below which the coverage does not increase with increasing exposure time [21]. These conclusions from STM data agreed with experiments using photoelectron spectroscopy and diffraction [101].

In addition to observing the (2 × 1), (2 × 2) and (1 × 1) structures of oxygen on W(1 1 0), Muzzall also observed a new structure by both STM and LEED [102]. An STM image of this new $\begin{pmatrix}3 & -1\\ 0 & 5\end{pmatrix}$ structure of W(1 1 0), which could be formed by exposing to 3 to 6L oxygen, is shown in figure 13(*e*). On the same sample, this new structure and the 2 × 1 structure could often be observed in different regions. The model proposed for this structure had 6 oxygen atoms per unit cell and a coverage of 0.40 ML.

7. Molecules adsorbed on metals

Three earlier reviews by the author about STM imaging of molecules have appeared previously [103–105].

7.1. Benzene and CO on Rh(1 1 1)

We decided to try imaging benzene and CO coadsorbed together on Rh(1 1 1) because Mate and Somorjai had found that CO induced ordering of the benzene molecules on Rh(1 1 1), resulting in a strongly chemisorbed layer [106]. Two different ordered overlayers can form, a (3 × 3) hexagonal structure and a $c(2\sqrt{3} \times 4)$ rect one. Hiroko Ohtani, a Japanese graduate student from UC Berkeley, came to work with us on these experiments. When we observed the first pictures of individual molecules on a surface, our STM images of the 3 × 3 overlayer attracted much attention, even from the popular press, because they showed clearly the ring structure of the benzene molecules (figure 14(*a*)) [107]. Of course, Kekulé had determined the structure of the benzene ring over a century before [108], after having had his famous dream of a snake chasing its tail. The rings in our STM image were not completely round, however, because the molecule is bonded to the metal surface, resulting in the molecular shape appearing somewhat triangular in the images. The LEED model of Lin, Van Hove and Somorjai (figure 14(*b*)) [109] even suggested some very small atomic distortions in the benzene ring, but the STM data could not confirm these because they are sensitive to the electronic structure rather than the atomic positions. The structural model showed one benzene model and two CO molecules per unit cell, with the CO molecules bonded vertically in three-fold hollow sites with the carbon atom nearer to the surface. In addition to the benzene rings, the STM images only show a protrusion at the location of one of the CO sites, whereas the other CO site seems to be occluded by part of the benzene ring.

The $c(2\sqrt{3} \times 4)$ rect overlayer of benzene and CO on Rh(1 1 1) has one benzene and one CO molecule per unit cell (figure 14(*e*)) [110]. For this overlayer, we were able to obtain high resolution STM images, with the benzene

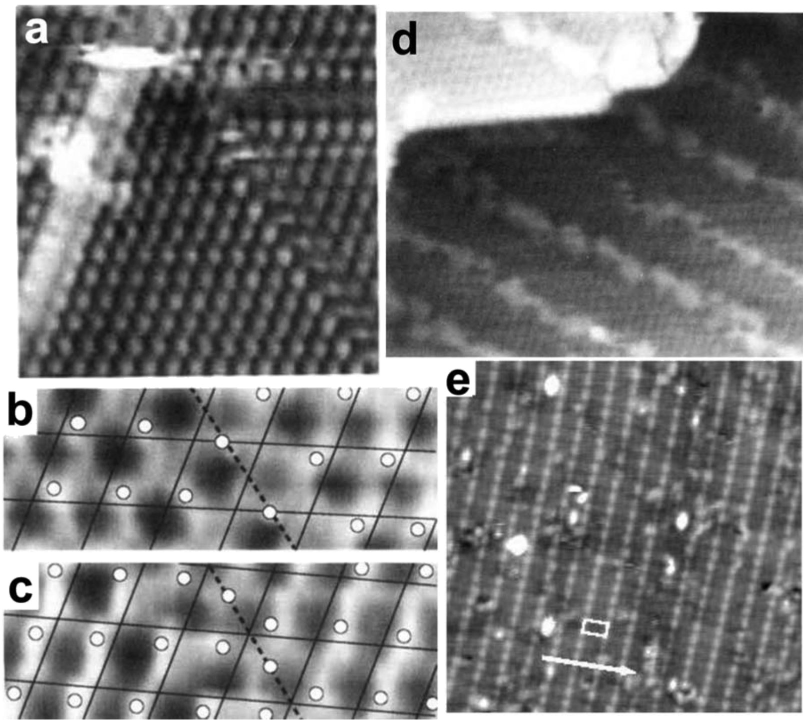

Figure 13. STM images of oxygen adsorbed on W(1 1 0). Note that oxygen atoms are imaged as depressions. (*a*) Saturated layer with coverage of 1 ML, $V_S = -10$ mV, $I_T = 1$ nA. Measured corrugation ≈ 0.7 Å. (*b*) and (*c*) Site-exchanged (1 × 1) domain walls in the [0 0 1] direction. Images are inverted, so that oxygen atoms appear bright. Solid lines indicate substrate lattice, broken line the domain wall, and open circles the O adsorption site. (*b*) Light wall with local site density less than in domain and (*c*) heavy wall with greater density. At both types of walls, an additional row of O adsorbs between domains in an intermediate site. (*d*) STM image of the superstructure of site-exchanged (1 × 1) domains after annealing the surface to 1250 K. $V_S = 1$ V, $i_T = 1$ nA. Domain corrugation ≈0.3 Å with walls ≈0.6 Å tall. (*e*) STM image of new $\begin{pmatrix} 3 & -1 \\ 0 & 5 \end{pmatrix}$ structure of W(1 1 0) dosed with 6L oxygen. The small rectangle indicates the unit cell of the new structure, and the arrow indicates the direction of its long axis. Area 200 Å × 200 Å, $V_S = -0.8$ V, $I_T = 0.8$ nA. (*a*)–(*d*) reprinted with permission from [96]. Copyright 1993 American Physical Society. (*e*) reprinted with permission from [102]. Copyright 2000 Materials Research Society.

molecules appearing as triangular rings and one protrusion in the unit cell appearing at site expected for CO [111]. Since this molecular arrangement is rectangular on a hexagonal lattice, three different rotational domains can occur on the surface and were observed in the images, together with domain boundaries and the arrangement of molecules near the step edges [112].

7.2. Copper phthalocyanine on Cu(1 0 0)

The first STM images showing the internal structure of individual molecules adsorbed on a surface were obtained for copper phthalocyanine (Cu-phth) on Cu(1 0 0) [113]. The model of the molecule on the rotated copper lattice is shown in figure 15(*a*). The Cu-phth molecules were adsorbed in a flat orientation on the surface in two different rotational orientations. The internal structure observed in the STM images showed strong resemblance to charge density contours at 2 Å above the molecular plane for the highest occupied molecular orbital (HOMO) and lowest unoccupied molecular orbital (LUMO) of the isolated molecule, which were both calculated using simple Hückel theory. Figure 15(*b*) shows the HOMO embedded into the high resolution STM image, which shows the internal structure of several individual molecules for submonolayer coverage. The inequivalent images for the two rotational orientations of the molecule in this image may result from a strong tip asymmetry. Figure 15(*c*) shows an additional high resolution image near 1 ML coverage; other images at this coverage show packed molecular arrays, usually with two rotational domains, consistent with previous LEED data [114]. Tip induced motion of molecules was occasionally observed, as were isolated molecules above an atomically resolved metal surface.

7.3. Naphthalene, azulene and methylazulenes on Pt(1 1 1)

We then examined naphthalene, which consists of two adjoining benzene rings, on Pt(1 1 1). LEED studies had previously found that annealing produced an ordered molecular layer characterized by a (6 × 3) pattern with a glide plane, leading to a proposed herringbone arrangement of the molecules [115, 116]. In most STM images, the naphthalene molecules appeared as double-lobed or oblong structures in three rotational orientations (figure 16(*d*)). They were organized in quasi-3 × 3 arrays, with about 40% of the molecules satisfying the required glide plane symmetry [117]. We also examined other regions of both ordered and disordered naphthalene on Pt(1 1 1) [118].

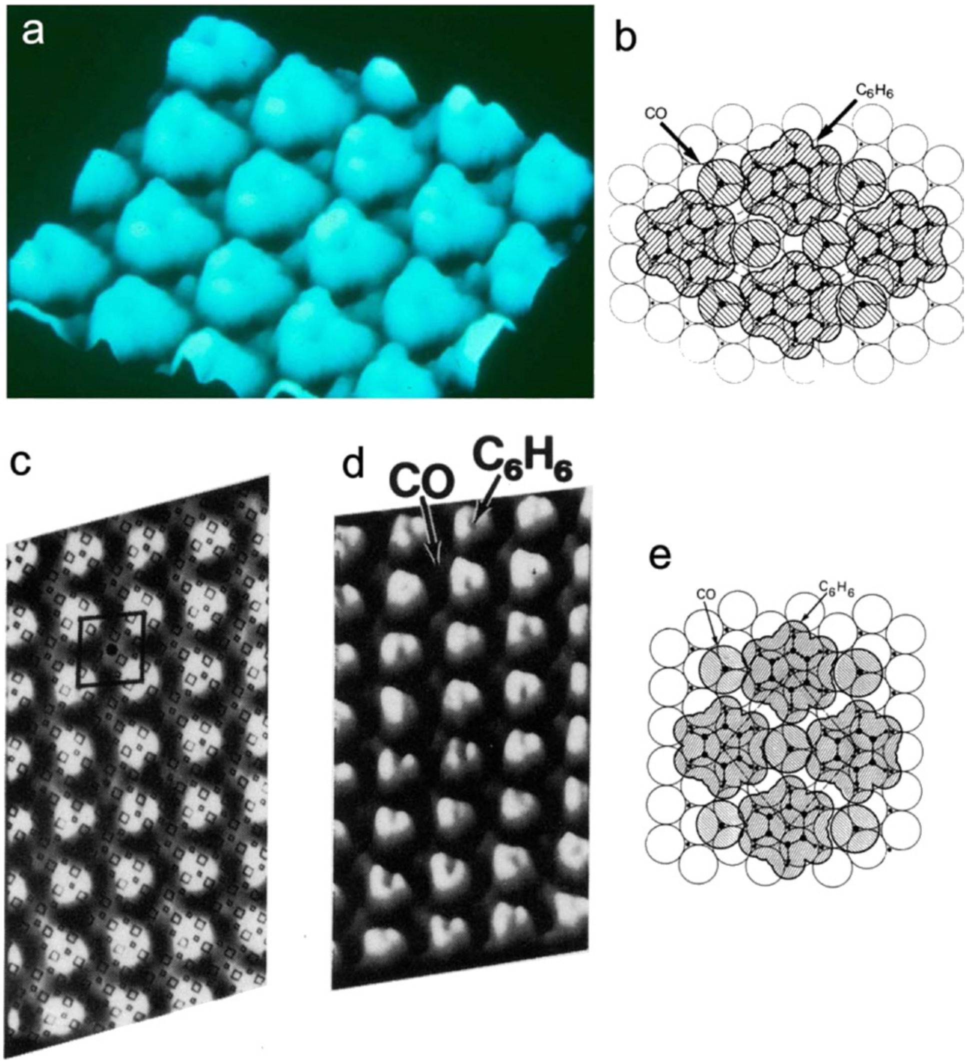

Figure 14. Benzene co-adsorbed with CO on Rh(1 1 1). (*a*) 3D view of STM image of the 3 × 3 overlayer, with ringlike benzene molecules. (*b*) 3 × 3 structure determined by LEED [109]. Large circles and small dots represent first- and second-layer metal atoms, respectively. (*c*) Top view of STM image of the $c(2\sqrt{3} \times 4)$ rect overlayer, with brightness proportional to height. The mesh, with large (small) diamonds indicating top (second) layer Rh atoms, was overlaid on the data according to the LEED model [110]. Solid lines show primitive unit cell, with benzenes at corners and CO molecule in centre. (*d*) 3D view of the data shown in (*c*), with three-fold benzene features ∼0.6 Å high and smaller CO protrusions ∼0.2 Å high. (*e*) $c(2\sqrt{3} \times 4)$ LEED model, with same symbols as in (*b*). (*a*)–(*b*) reprinted with permission from [107]. Copyright 1988 American Physical Society. (*c*)–(*e*) reprinted with permission from [111]. Copyright 1988 John Wiley and Sons.

Subsequently, we decided to compare two isomers on the Pt(1 1 1) surface, naphthalene and azulene, which consists of a 7-membered ring connected to a 5-membered ring [119]. By comparing STM images of these two molecules measured with the same tip, we were able to isolate the influence of the tip on the observed resolution of the molecules. Azulene usually appeared as a round disc, without other distinguishing features (figure 16(*h*)). We estimated the ratio of sticking coefficients for naphthalene to azulene is 4. From changes in the STM images, we observed evidence for molecular motion at room temperature. Very occasionally, with a particularly good tip, the naphthalene molecules appear as double rings (figure 16(*e*)), while azulenes appear as single rings (figure 16(*i*)) [120].

We began to do a systematic study of STM imaging of related molecules on Pt(1 1 1). These included not only naphthalene and azulene, but a series of azulene isomers with substituted methyl groups, which we obtained from collaborators Meinhardt and Hafner at Darmstadt. We measured three isomers of monomethylazulene, plus dimethyl- and trimethyl- azulene. We found that 1-methyl azulene appeared to have a shape like a kidney bean, while 2-methyl azulene appeared to be pear-shaped (figure 16(*p*)) [120]. We obtained somewhat higher resolution images showing some internal molecular features for 6-methylazulene (figure 16(*q*)) [121, 122]. We also used the STM data to study molecular resolution effects and to determine adsorption parameters for these molecules [121]. Trimethylazulene usually appeared like a clover leaf with one bright lobe (figure 16(*v*)), while dimethylazulene appeared as a distorted oblong with a bright spot (figure 16(*w*)). Note that, empirically, we usually seemed to obtain better molecular images when imaging empty states of the sample.

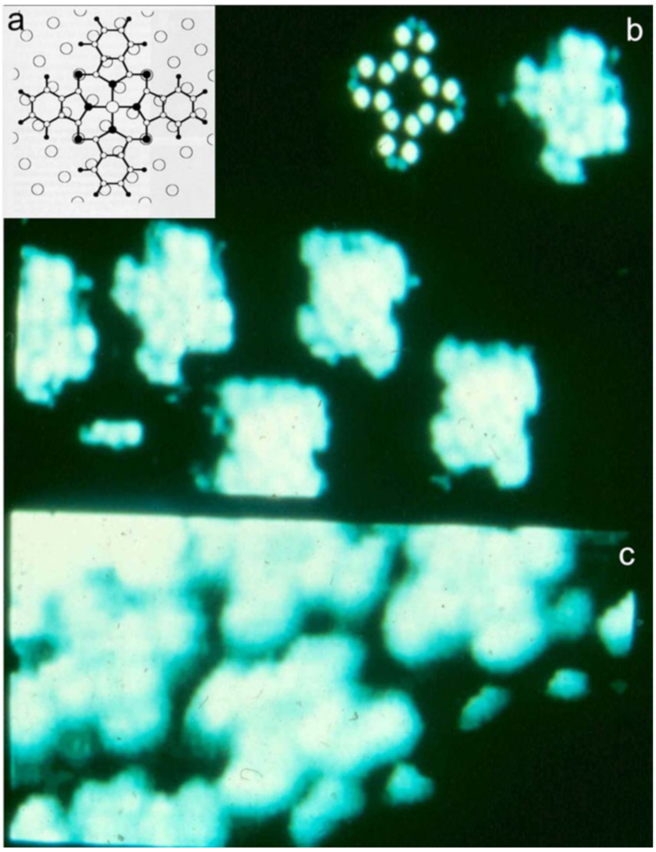

Figure 15. (*a*) Model of the Cu-phthalocyanine molecule above a Cu(1 0 0) surface. Small (large) open circles are C (Cu) atoms and small (large) filled circles are H (N) atoms. The Cu(1 0 0) lattice is shown rotated by 26.5°. (*b*) High-resolution STM image of Cu-phthalocyanine molecules on Cu(1 0 0) at submonolayer coverage, $V_T = -0.15$ V, $i_T = 2$ nA. Fine structure has been emphasized by baseline subtraction, and a greyscale representation of the HOMO, evaluated 2 Å above the molecular plane, has been embedded in the image. (*c*) High-resolution image near 1 ML coverage with $V_T = -0.07$ V, $i_T = 6$ nA. Reprinted with permission from [113]. Copyright 1989 American Physical Society.

7.4. Calculations of predicted STM images of molecules on metal surfaces

Meanwhile, we continued to develop our simple Hückel calculations to simulate STM images for molecules on metal surfaces. We calculated only the LDOS, using a molecule plus a cluster of metal atoms, assuming that the Tersoff and Hamann model for theory of STM was sufficient [7, 8]. Our calculations thus had no tip and no tunnelling process. We found that calculations of the LUMO or HOMO for isolated molecules did not fit the observed STM images as well as simulations which included a cluster of metal atoms. This behaviour was particularly striking for simulated images of the monomethylazulenes [122]. For low resolution data, we computed the LDOS at a height of 2 Å above the molecule, while for higher resolution data, we computed the LDOS at a height of 0.5 Å above the molecule. This method worked quite well in comparing the calculations (figures 16(*b*) and (*c*)) with the corresponding data for naphthalene at low and high resolution (figures 16(*d*) and (*e*)). In addition, calculated images for other molecules are shown in figures 16(*g*), (*k*), (*m*), (*o*), (*s*) and (*u*).

We presented a more systematic study of the parameters for the Hückel calculations in another paper [11]. Here we considered the effects of different adsorption geometries and different sizes, shapes and number of layers for the metal clusters. In addition, we considered the effect of different numbers of molecular orbitals, either empty or filled, to simulate the effects of the bias voltage.

We also computed molecular images for other systems. For xylene (benzene with two substituted methyl groups) on Rh(1 1 1), our calculated images from Hückel theory [123] agreed well with experiments from Salmeron's group [124]. In addition, we calculated predicted STM images for benzene on Pt(1 1 1), benzene on Pd(1 1 1), thiophene on Pd(1 1 1) [125], and furan and pyrrole on Pd(1 1 1) [126].

Sautet and Joachim developed their electron scattering quantum chemistry (ESQC) theory to simulate STM images of molecules, applying it first to benzene on Rh(1 1 1) [127]. Their calculated images agreed very well with our data [107, 111]. Later, Weiss and Eigler observed different shapes for benzene on Pt(1 1 1) at 4 K which appeared to depend on the binding site of the molecule [128]. Sautet's theory was able to simulate and explain this site dependence [129].

7.5. Benzene and CO on Pd(1 1 1)

Postdoctoral fellows Chris Pearson and Geoff Anderson measured STM images of benzene and CO coadsorbed on Pd(1 1 1) at low temperature [19], and they found many similarities to the cases of co-adsorption of these molecules on Rh(1 1 1). If they first deposited CO onto the Pd(1 1 1) surface, it acted as an ordering agent. Two different ordered structures can form when CO and benzene are subsequently dosed onto the surface simultaneously. For low benzene coverage, they observed a $(2\sqrt{3} \times 2\sqrt{3})$R30° LEED pattern, followed by a 3 × 3 pattern for higher benzene coverage. An STM image of the $(2\sqrt{3} \times 2\sqrt{3})$R30° overlayer is shown in figure 17(*a*), with individual benzene molecules clearly resolved. If the Pd(1 1 1) surface is dosed first with benzene, and then with CO and benzene together, a rectangular structure forms on the surface. Three rectangular domains are clearly observed in figure 17(*b*) [19].

7.6. Xylene on Pd(1 1 1)

Graduate students Don Futaba and Al Loui and undergraduate student Jin Landry studied the adsorption of xylene on Pd(1 1 1), both experimentally and theoretically. Images of metaxylene and paraxylene on Pd(1 1 1) show very different molecular shapes. Metaxylene appears somewhat triangular and prefers to adsorb along step edges [130]. Paraxylene forms more ordered arrays on the surface, with the shape of the adsorbed molecule, however, being asymmetric (figure 18(*b*)). Comparing with our Hückel calculations for the molecule on a Pd cluster, the molecular shape seems closest to the simulated image for an angle of 15° between the molecular axis

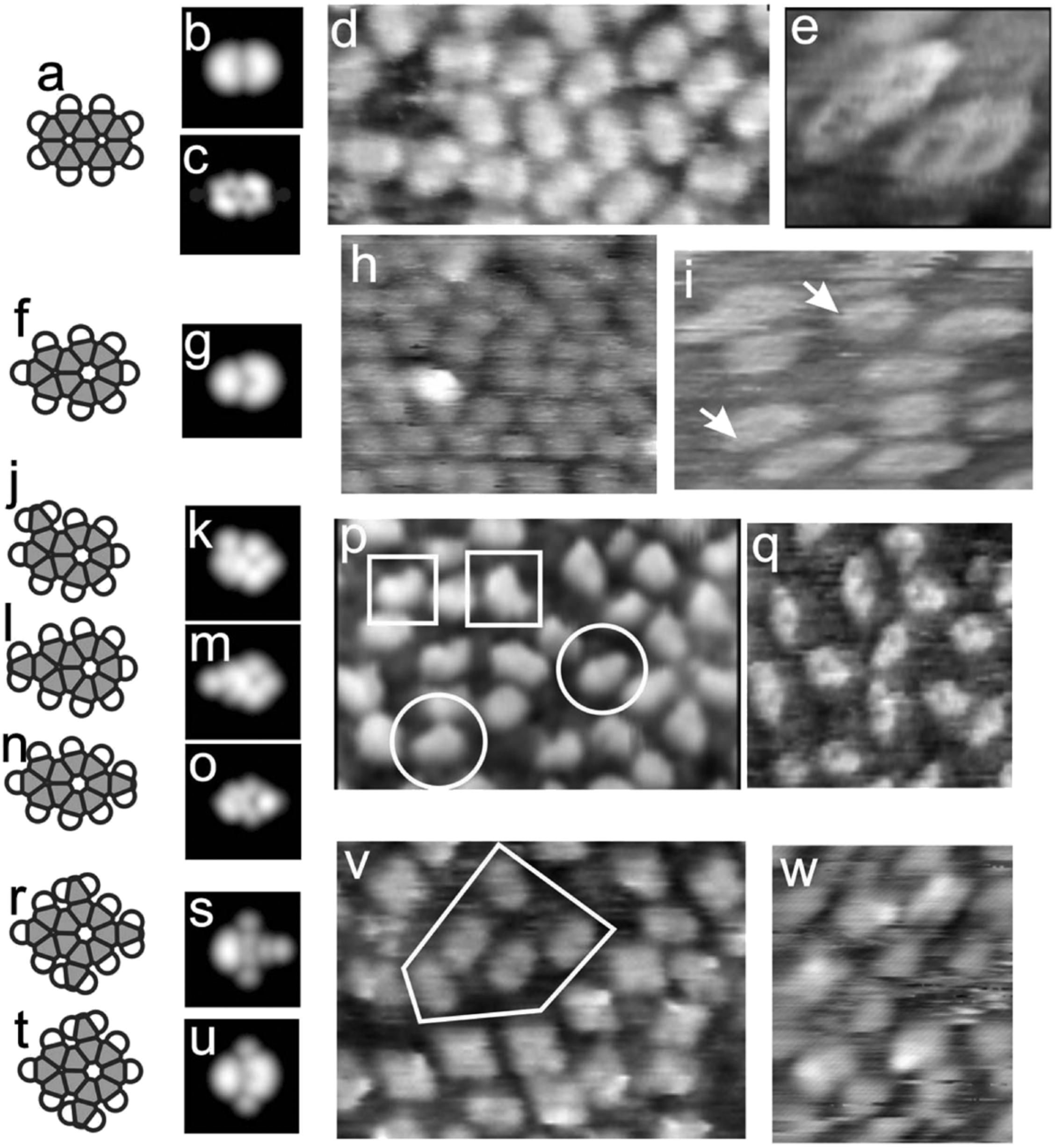

Figure 16. Predicted and actual STM images for a series of related molecules on Pt(1 1 1). (*a*) Naphthalene diagram. (*b*) naphthalene ρ_H (LDOS of unoccupied sample states) at 2 Å above the molecule. (*c*) naphthalene ρ_H at 0.5 Å. (*d*) Low resolution image of array of naphthalene molecules. Molecular Van der Waals length is 8.1 Å. (*e*) High resolution STM image of naphthalene. (*f*) Azulene model. (*g*) Azulene ρ_H at 2 Å. (*h*) Low resolution azulene data near 1 ML coverage. Molecular spacing within a (3 × 3) domain is 8.3 Å. (*i*) High resolution STM image of mixed molecular layer, with two azulenes (marked by arrows) among naphthalene neighbours. (*j*) 1-methylazulene (1-MA) model. (*k*) 1-MA ρ_H at 2 Å. (*l*) 2-MA model. (*m*) 2-MA ρ_H at 2 Å. (*n*) 6-MA model. (*o*) 6-MA ρ_H at 0.5 Å. (*p*) Low resolution image of mixed 1-MA, ~ 20% coverage (in squares) and 2-MA (in circles) near saturation coverage. (*q*) High resolution image of 6-MA (*r*) 4,6,8-trimethylazulene (TMA) model. (*s*) TMA ρ_H at 2 Å. (*t*) 4,8-dimethylazulene (DMA). (*u*) DMA ρ_H at 2 Å. (*v*) STM image for mixed TMA and naphthalene (inside marked area) layer. (*w*) STM image of DMA molecules at less than full coverage; noisy areas indicate molecules which move during the scan duration. Reprinted with permission from [122]. Copyright 1993 American Physical Society.

and the overlayer close-packed direction (figure 18(*a*)) [131]. The energy calculations suggest that the molecules adsorb on hollow sites an angles between 15° and 30° with respect to the substrate close-packed direction. Experimentally, the angle between the close-packed direction of the overlayer structure and the orientation of the paraxylene molecules was measured to be 15° ± 5.2°, which is consistent with the calculations.

7.7. *Furan decomposition on Pd(1 1 1)*

Loui used STM to study the adsorption and decomposition of furan on Pd(1 1 1) [132]. Furan appears in STM images as a heart-shaped molecule, which prefers to adsorb along the step edges with the O atom oriented either towards or away from the step. Figure 19 shows an STM image of furan molecules near a Pd step, together with the predicted

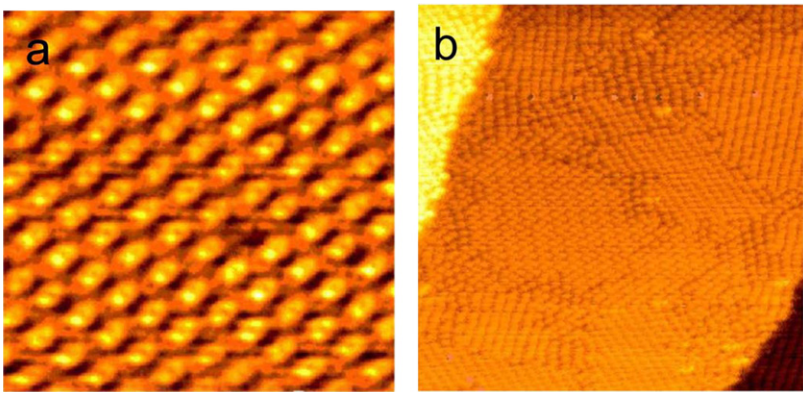

Figure 17. (*a*) A 100 Å × 100 Å STM image of the $(2\sqrt{3} \times 2\sqrt{3})$R30° structure of CO and benzene coadsorbed on Pd(1 1 1), measured at 95 K. The ordered arrangement and internal ring-like structure of the benzene molecules is clearly evident in the image. $V_S = 0.1$ V, $I_T = 0.7$ nA. (*b*) A 250 Å × 250 Å STM image of the three domain rectangular structure of CO and benzene coadsorbed on Pd (1 1 1), measured at 100 K. The benzene molecules are tightly arranged within each domain, while the domain boundaries display disorder. $V_S = 0.1$ V, $I_T = 0.5$ nA (*b*) reprinted with permission from [19]. Copyright 2002 Elsevier.

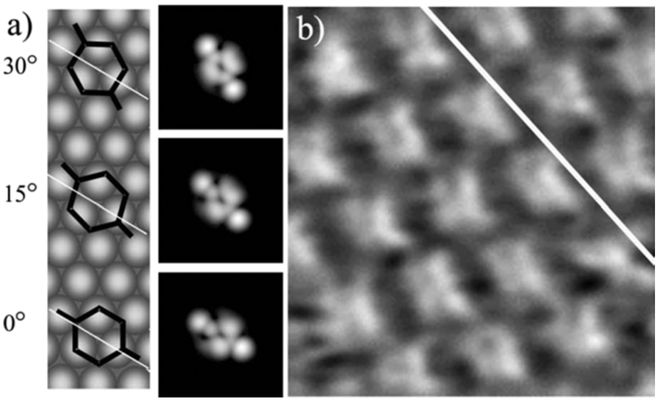

Figure 18. Schematic drawings illustrating the relative molecular orientation for paraxylene on the surface and associated calculated images, for decreasing angular difference between the molecular axis and the overlayer close-packed direction denoted in white. As the angular difference decreases, the image displays an increasingly symmetric profile. (*b*) STM image of paraxylene molecules, with the overlayer close-packed direction denoted in white. Reprinted with permission from [131]. Copyright 2002 American Physical Society.

STM image, calculated from Hückel theory [126]. Land's group had previously studied the decomposition reaction of furan on Pd(1 1 1) and found evidence that it decomposes just above room temperature into H, CO and a C_3H_3 fragment on the surface [133]. Around 350 K, two C_3H_3 fragments dimerize to form benzene, although the process has rather low yield. Loui measured this process using a low temperature STM. He observed adsorption and diffusion of furan molecules at low temperature. Above room temperature, he observed some molecular species which were consistent with C_3H_3 fragments [134, 135]. He also performed DFT calculations on furan adsorbed on Pd(1 1 1) and for C_3H_3 on Pd(1 1 1) [134, 136]. Woodruff's group has recently studied this system using photoelectron diffraction, near edge x-ray adsorption fine structure, and DFT [137–140].

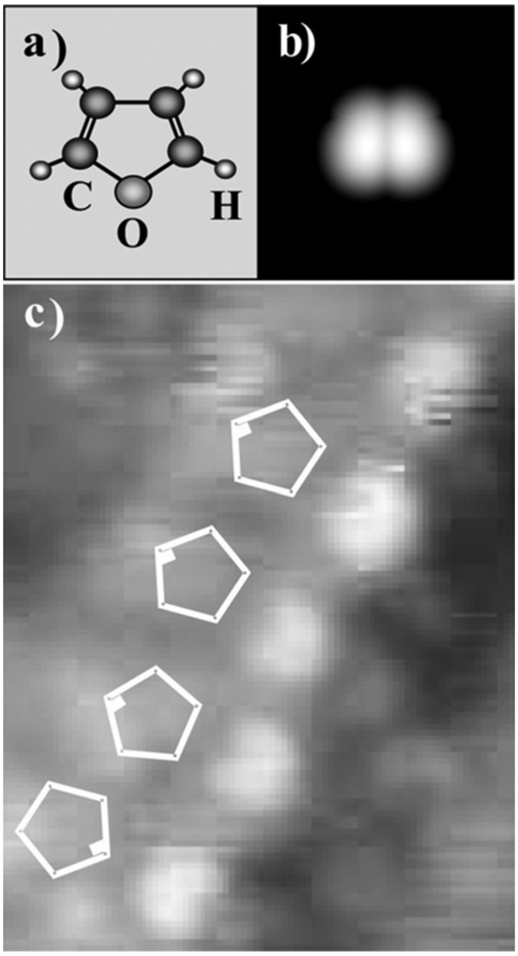

Figure 19. (*a*) Schematic representation of furan molecule, with atomic species indicated. (*b*) Base 10 logarithmic plot of integrated Fermi-level electron density at 2 Å above molecular plane [126]. (*c*) 30 Å × 50 Å STM image of furan on Pd(1 1 1) at 225 K. The features populating the upper step edge are chiefly oriented with the heteroatom facing towards the terrace. Pentagons representing the furan molecule, with the oxygen atom marked, are added to guide the eye. $V_S = -1.0$ V, $I_T = 0.13$ nA. Reprinted with permission from [132]. Copyright 2004 Elsevier.

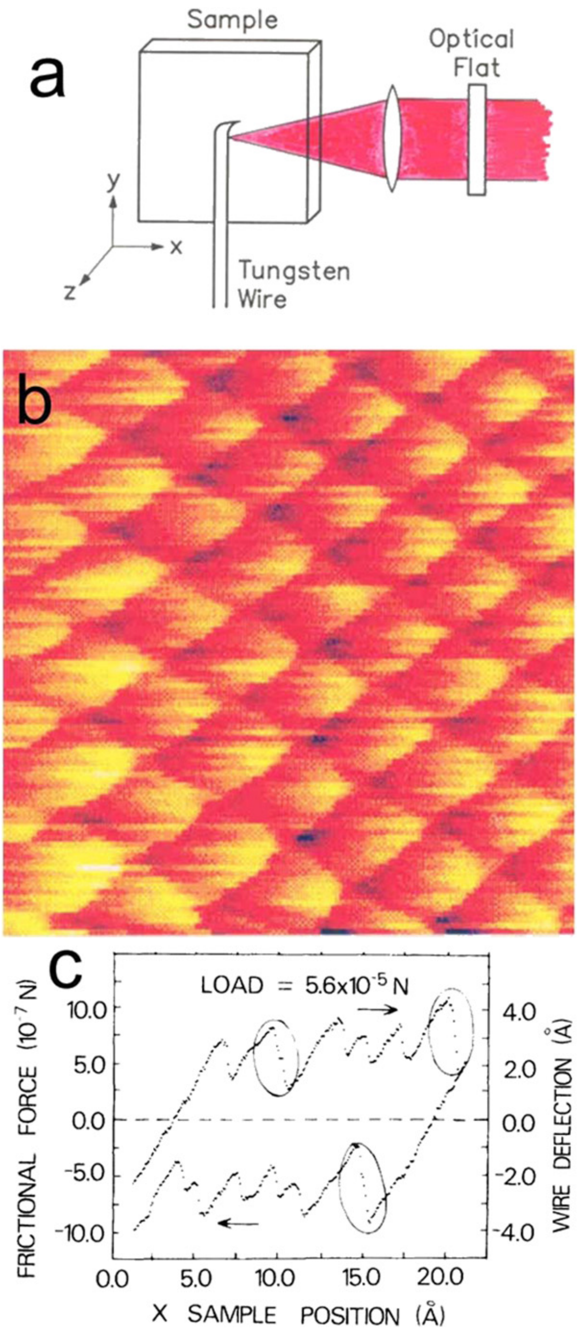

Figure 20. (*a*) Schematic diagram of apparatus for measuring friction on surface with AFM. The base of the tungsten wire is held fixed, while the sample is moved in the x, y and z directions. Wire deflections parallel to the surface are measured from the intensity change in the interference pattern between light reflected off the wire and light reflected off the optical flat. (*b*) Top view shows frictional force in the x- direction as a function of sample position in x and y. Image intensity is proportional to frictional force, with bright areas corresponding to high force, and the full-scale change from dark to bright corresponding to 1.8×10^{-6} N. Only scans in the left-to right direction are shown. Image size 20 Å × 20 Å. Tip load 5.6×10^{-5} N, and wire spring constant was 2500 N m^{-1}. (*c*) Wire deflection parallel to the surface and the corresponding frictional force on the tip as a function of sample position for specified load. The circled sections indicate double slips. Reprinted with permission from [141]. Copyright 1987 American Physical Society.

8. Friction on graphite and mica

We decided to use our AFM with the optical interference detection of the lever deflection to measure the lateral forces on a tip sliding tip near a graphite surface (figure 20(*a*)). We observed atomic scale features in measurements of the frictional force for a tungsten tip sliding over the basal plane of graphite for low loads, $<10^{-4}$ N (figure 20(*c*)) [141]. The frictional force displayed a pattern of atomic scale slips which had a lateral periodicity of ~2.5 Å, which is the same periodicity as the honeycomb structure of the graphite lattice. When the frictional force in the x-direction was plotted as a top view image as a function of relative position of the sample with respect to the tip, the atomic features had the periodicity of the graphite lattice (figure 20(*b*)). Measurements of the frictional force on mica surfaces showed similar atomic scale behaviour, with the frictional force varying laterally with the periodicity of the hexagonal layer of the SiO_4 units which form the cleavage plane of the mica [142].

We also used our AFM to directly measure the normal force between a Pt–Rh tip and a graphite sample during STM measurements in air [143]. We found that forces in the range 10^{-7}–10^{-6} N were required to maintain tunnelling, and that the force to maintain a tunnelling current depended on the position of the tip with respect to the graphite unit cell. 'Giant corrugations' had previously been observed for STM images of graphite [144–146], and several explanations of the phenomena had been advanced [144, 145, 147]. Our measurements of the forces during STM imaging of graphite were consistent with the contamination mediated deformation model presented by Mamin *et al* [144]. Nevertheless, we could not rule out Pethica's model involving the sliding of a graphite flake across the surface [147].

Acknowledgments

I am pleased to thank all of my wonderful collaborators who assisted with the work described above, over nearly 30 years. First, I want to thank the group at IBM Almaden, from 1983 to 1994: particularly Robert Wilson, Vickie Hallmark, David Chambliss, Christof Wöll, Sylvie Rousset, David Fowler, Philip Lippel, Hiroko Ohtani, Frank Salvan, Kevin Johnson, Jonathan Mamin, Kathrin Kalki, Gary McClelland, Mathew Mate, Ragnar Erlandsson, K-P, Meinhardt and K. Hafner. Secondly, I want to thank my students and postdoctoral fellows at UC Davis who contributed to the work described above, beginning in 1994: Don Futaba, David Muzzall, Gayle Thayer, Albert Loui, Jim Landry, Chris Pearson and Geoff Anderson. I am pleased to acknowledge support from the National Science Foundation under Grant CHE-071954 for our current research on metals on semiconductors.

References

[1] Binnig G and Rohrer H 1982 *Helv. Phys. Acta* **55** 726–35
[2] Binnig G, Rohrer H, Gerber C and Weibel E 1982 *Phys. Rev. Lett.* **49** 57
[3] Binnig G and Rohrer H 1983 *Surf. Sci.* **126** 236–44
[4] Binnig G and Rohrer H 1983 *Ultramicroscopy* **11** 157–60

[5] 'Press release: The 1986 nobel prize in physics'. 15 October 1986 http://nobelprize.org/nobel_prizes/physics/laureates/1986/press.html

[6] Van Hove M A, Weinberg W H and Chan C-M 1986 *Low-Energy Electron Diffraction: Experiment, Theory, and Surface Structure Determination* vol 6 (Berlin: Springer)

[7] Tersoff J and Hamann D R 1983 *Phys. Rev. Lett.* **50** 1998

[8] Tersoff J and Hamann D R 1985 *Phys. Rev.* B **31** 805

[9] Hallmark V M, Chiang S, Rabolt J F, Swalen J D and Wilson R J 1987 *Phys. Rev. Lett.* **59** 2879–82

[10] Feenstra R M, Stroscio J A, Tersoff J and Fein A P 1987 *Phys. Rev. Lett.* **58** 1192–5

[11] Hallmark V M and Chiang S 1995 *Surf. Sci.* **329** 255–68

[12] Binnig G, Quate C F and Gerber C 1986 *Phys. Rev. Lett.* **56** 930–3

[13] Binnig G, Rohrer H, Gerber C and Weibel E 1983 *Phys. Rev. Lett.* **50** 120–3

[14] Chiang S, Wilson R J, Gerber C and Hallmark V M 1988 *J. Vac. Sci. Technol.* A **6** 386–9

[15] Erlandsson R, Mcclelland G M, Mate C M and Chiang S 1988 *J. Vac. Sci. Technol.* A **6** 266–70

[16] Gerber C, Binnig G, Fuchs H, Marti O and Rohrer H 1986 *Rev. Sci. Instrum.* **57** 221–4

[17] Müller E W and Tsong T T 1969 *Field Ion Microscopy, Principles and Applications* (New York: Elsevier)

[18] Chiang S and Wilson R J 1986 *IBM J. Res. Dev.* **30** 515–9

[19] Pearson C, Anderson G W, Chiang S, Hallmark V M and Melior B J 2002 *Mater. Sci. Eng.* B **96** 209–14

[20] Poppenheimer E C 2011 *BS Dissertation* Physics, University of California, Davis, CA

[21] Muzzall D E 2001 *PhD Dissertation* Physics, University of California, Davis, CA

[22] Futaba D N 2000 *PhD Dissertation* Physics, University of California, Davis, CA

[23] Czap G 2011 *BS Dissertation* Physics, University of California, Davis, CA

[24] Binnig G and Rohrer H 1987 *Rev. Mod. Phys.* **59** 615–25

[25] Takayanagi K, Tanishiro Y, Takahashi M and Takahashi S 1985 *J. Vac. Sci. Technol.* A **3** 1502–6

[26] Takayanagi K, Tanishiro Y, Takahashi S and Takahashi M 1985 *Surf. Sci.* **164** 367–92

[27] Chiang S and Wilson R J 1987 *Anal. Chem.* **59** 1267A–70A

[28] Lelay G 1983 *Surf. Sci.* **132** 169–204

[29] Wilson R J and Chiang S 1987 *Phys. Rev. Lett.* **58** 369–72

[30] Van Loenen E J, Demuth J E, Tromp R M and Hamers R J 1987 *Phys. Rev. Lett.* **58** 373–6

[31] Wilson R J and Chiang S 1988 *J. Vac. Sci. Technol.* A **6** 398–400

[32] Wilson R J and Chiang S 1987 *Phys. Rev. Lett.* **59** 2329–32

[33] Takahashi T, Nakatani S, Okamoto N, Ishikawa T and Kikuta S 1988 *Japan. J. Appl. Phys. Part 2—Lett.* **27** L753–L5

[34] Takahashi T, Nakatani S, Okamoto N, Ishikawa T and Kikuta S 1991 *Surf. Sci.* **242** 54–8

[35] Takahashi T and Nakatani S 1993 *Surf. Sci.* **282** 17–32

[36] Sato N, Nagao T and Hasegawa S 1999 *Surf. Sci.* **442** 65–73

[37] Aizawa H, Tsukada M, Sato N and Hasegawa S 1999 *Surf. Sci.* **429** L509–L14

[38] Zhang H M, Gustafsson J B and Johansson L S O 2006 *Phys. Rev.* B **74** 201304(R)

[39] Stroscio J A, Feenstra R M and Fein A P 1986 *Phys. Rev. Lett.* **57** 2579–82

[40] Stroscio J A, Feenstra R M and Fein A P 1987 *J. Vac. Sci. Technol.* A **5** 838–41

[41] Feenstra R M and Stroscio J A 1987 *J. Vac. Sci. Technol. B* **5** 923–9

[42] Stroscio J A, Feenstra R M and Fein A P 1987 *Phys. Rev.* B **36** 7718–21

[43] Stroscio J A, Feenstra R M, Newns D M and Fein A P 1988 *J. Vac. Sci. Technol.* A **6** 499–507

[44] Hamers R J, Tromp R M and Demuth J E 1986 *Phys. Rev. Lett.* **56** 1972–5

[45] Wilson R J and Chiang S 1987 *Phys. Rev. Lett.* **58** 2575–8

[46] Parikh S A, Lee M Y and Bennett P A 1996 *Surf. Sci.* **356** 53–8

[47] Kinoda G and Ogawa K 2000 *Surf. Sci.* **461** 67–77

[48] Daugy E, Mathiez P, Salvan F and Layet J M 1985 *Surf. Sci.* **154** 267–83

[49] Chambers S A, Anderson S B and Weaver J H 1985 *Phys. Rev.* B **32** 581–7

[50] Wilson R J, Chiang S and Salvan F 1988 *Phys. Rev.* B **38** 12696–9

[51] Demuth J E, Koehler U K, Hamers R J and Kaplan P 1989 *Phys. Rev. Lett.* **62** 641–4

[52] Kawasaki T, An T, Ito H and Ichinokawa T 2001 *Surf. Sci.* **487** 39–48

[53] Zhang Y P, Yong K S, Chan H S O, Xu G Q, Gao X Y, Qi D C, Wang X S and Wee A T S 2008 *J. Phys. D: Appl. Phys.* **41** 095306

[54] Sato Y, Chiang S and Bartelt N C 2007 *Phys. Rev. Lett.* **99** 096103

[55] Sato Y and Chiang S 2009 *Surf. Sci.* **603** 2300–4

[56] Giacomo J A 2009 *PhD Dissertation* Physics, University of California, Davis, CA

[57] Mullet C H 2011 *PhD Dissertation* Physics, University of California, Davis, CA

[58] Reichelt K and Lutz H O 1971 *J. Cryst. Growth* **10** 103

[59] Binnig G, Rohrer H, Gerber C and Weibel E 1983 *Surf. Sci.* **131** L379–L84

[60] Binnig G K, Rohrer H, Gerber C and Stoll E 1984 *Surf. Sci.* **144** 321–35

[61] Harten U, Lahee A M, Toennies J P and Woll C 1985 *Phys. Rev. Lett.* **54** 2619–22

[62] Wöll C, Chiang S, Wilson R J and Lippel P H 1989 *Phys. Rev.* B **39** 7988–91

[63] Chambliss D D and Wilson R J 1991 *J. Vac. Sci. Technol.* B **9** 928–32

[64] Barth J V, Brune H, Ertl G and Behm R J 1990 *Phys. Rev.* B **42** 9307–18

[65] Potschke G O and Behm R J 1991 *Phys. Rev.* B **44** 1442–5

[66] Eigler D M and Schweizer E K 1990 *Nature* **344** 524–6

[67] Mamin H J, Chiang S, Birk H, Guethner P H and Rugar D 1991 *J. Vac. Sci. Technol.* B **9** 1398–402

[68] Chambliss D D, Wilson R J and Chiang S 1991 *Phys. Rev. Lett.* **66** 1721–4

[69] Chambliss D D, Wilson R J and Chiang S 1991 *J. Vac. Sci. Technol.* B **9** 933–7

[70] Stroscio J A, Pierce D T, Dragoset R A and First P N 1992 *J. Vac. Sci. Technol.* A **10** 1981–5

[71] Chambliss D D, Wilson R J and Chiang S 1995 *IBM J. Res. Dev.* **39** 639–54

[72] Palmberg P W and Rhodin T N 1968 *J. Chem. Phys.* **49** 134–46

[73] Chambliss D D and Chiang S 1992 *Surf. Sci.* **264** L187–L92

[74] Wang Z Q, Li Y S, Lok C K C, Quinn J, Jona F and Marcus P M 1987 *Solid State Commun.* **62** 181–5

[75] Fenter P and Gustafsson T 1990 *Phys. Rev. Lett.* **64** 1142–5

[76] Fenter P and Gustafsson T 1991 *Phys. Rev.* B **43** 12195–204

[77] Rousset S, Chiang S, Fowler D E and Chambliss D D 1992 *Phys. Rev. Lett.* **69** 3200–3

[78] Rousset S, Chiang S, Fowler D E and Chambliss D D 1993 *Surf. Sci.* **287** 941–5

[79] Chiang S, Rousset S, Fowler D E and Chambliss D D 1994 *J. Vac. Sci. Technol.* B **12** 1747–50

[80] Bohnen K P, Chan C T and Ho K M 1992 *Surf. Sci.* **268** L284–L6

[81] Chan C T, Bohnen K P and Ho K M 1992 *Phys. Rev. Lett.* **69** 1672–5

[82] Haftel M I, Rosen M, Franklin T and Hettermann M 1994 *Phys. Rev. Lett.* **72** 1858–61

[83] Haftel M I and Rosen M 1995 *Phys. Rev.* B **51** 4426–34

[84] Wang R P and Fichthorn K A 1995 *Phys. Rev.* B **51** 1957–60

[85] Hirschorn E S, Lin D S, Hansen E D and Chiang T C 1995 *Surf. Sci.* **323** L299–L304

[86] Johnson K E, Chambliss D D, Wilson R J and Chiang S 1994 *Surf. Sci.* **313** L811–L6

[87] Chambliss D D, Johnson K E, Kalki K, Chiang S and Wilson R J 1993 *Magnetic Ultrathin Films. Multilayers and Surfaces, Interfaces and Characterization Symposium.* ed B T Jonker *et al* (Philadelphia, PA: Materials Research Society) vol 313 pp 713–22

[88] Kalki K, Chambliss D D, Johnson K E, Wilson R J and Chiang S 1993 *Phys. Rev.* B **48** 18344–7

[89] Thayer G E, Ozolins V, Schmid A K, Bartelt N C, Asta H, Hoyt J J, Chiang S and Hwang R Q 2001 *Phys. Rev. Lett.* **86** 660–3

[90] Thayer G E, Bartelt N C, Ozolins V, Schmid A K, Chiang S and Hwang R Q 2002 *Phys. Rev. Lett.* **89** 036101

[91] Zeng H C, McFarlane R A, Sodhi R N S and Mitchell K A R 1988 *Can. J. Chem.—Rev. Can. Chim.* **66** 2054–62

[92] Wöll C, Wilson R J, Chiang S, Zeng H C and Mitchell K A R 1990 *Phys. Rev.* B **42** 11926–9

[93] Germer L H and May J W 1966 *Surf. Sci.* **4** 452–70

[94] Engel T, Niehus H and Bauer E 1975 *Surf. Sci.* **52** 237–62

[95] Bauer E and Engel T 1978 *Surf. Sci.* **71** 695–718

[96] Johnson K E, Wilson R J and Chiang S 1993 *Phys. Rev. Lett.* **71** 1055–8

[97] Lang N D 1986 *IBM J. Res. Dev.* **30** 374–9

[98] Lang N D 1987 *Phys. Rev. Lett.* **58** 45–8

[99] Lang N D 1989 *Comment. Condens. Matter Phys.* **14** 253

[100] Bauer E 1967 *Surf. Sci.* **7** 351–64

[101] Ynzunza R X *et al* 2000 *Surf. Sci.* **459** 69–92

[102] Muzzall D E and Chiang S 2000 *Recent Developments in Oxide and Metal Epitaxy—Theory and Experiment. Symp. (Materials Research Society Symposium Proceedings)* ed M Yeadon *et al* (Warrendale, PA: Materials Research Society) vol 619 pp 57–61

[103] Chiang S 1997 *Chem. Rev.* **97** 1083–96

[104] Chiang S 1992 *Scanning Tunneling Microscopy I* ed H-J Güntherodt and R Wiesendanger (Berlin: Springer) pp 181–205

[105] Chiang S 1994 *Scanning Tunneling Microscopy I* ed H-J Güntherodt and R Wiesendanger (New York: Springer) pp 258–67

[106] Mate C M and Somorjai G A 1985 *Surf. Sci.* **160** 542–60

[107] Ohtani H, Wilson R J, Chiang S and Mate C M 1988 *Phys. Rev. Lett.* **60** 2398–401

[108] Kekulé A 1865 *Bull. Soc. Chim. Paris* **3** 98–110

[109] Lin R F, Blackman G S, Vanhove M A and Somorjai G A 1987 *Acta Crystallogr. Sect.* B **43** 368–76

[110] Van Hove M A, Lin R F and Somorjai G A 1986 *J. Am. Chem. Soc.* **108** 2532–7

[111] Chiang S, Wilson R J, Mate C M and Ohtani H 1988 *J. Microsc.—Oxford* **152** 567–71

[112] Chiang S, Wilson R J, Mate C M and Ohtani H 1990 *Vacuum* **41** 118–20

[113] Lippel P H, Wilson R J, Miller M D, Woll C and Chiang S 1989 *Phys. Rev. Lett.* **62** 171–4

[114] Buchholz J C and Somorjai G A 1977 *J. Chem. Phys.* **66** 573–80

[115] Dahlgren D and Hemminger J C 1981 *Surf. Sci.* **109** L513–L8

[116] Dahlgren D and Hemminger J C 1982 *Surf. Sci.* **114** 459–70

[117] Hallmark V M, Chiang S, Brown J K and Wöll C 1991 *Phys. Rev. Lett.* **66** 48–51

[118] Hallmark V M, Chiang S and Wöll C 1991 *J. Vacu. Sci. Technol. B* **9** 1111–4

[119] Hallmark V M, Chiang S, Brown J K and Wöll C 1992 *Synthetic Microstructures in Biological Research* ed J M Schnur and M Peckerar (New York: Plenum) pp 79–90

[120] Hallmark V M and Chiang S 1993 *Surf. Sci.* **286** 190–200

[121] Chiang S, Hallmark V M, Meinhardt K P and Hafner K 1994 *J. Vac. Sci. Technol.* B **12** 1957–62

[122] Hallmark V M, Chiang S, Meinhardt K P and Hafner K 1993 *Phys. Rev. Lett.* **70** 3740–3

[123] Futaba D N and Chiang S 2000 *Surf. Sci.* **448** L175–L8

[124] Cernota P D, Yoon H A, Salmeron M and Somorjai G A 1998 *Surf. Sci.* **415** 351–62

[125] Futaba D N and Chiang S 1999 *Japan. J. Appl. Phys. Part 1—Regular Pap. Short Notes Rev. Pap.* **38** 3809–12

[126] Futaba D N and Chiang S 1997 *J. Vac. Sci. Technol.* A **15** 1295–8

[127] Sautet P and Joachim C 1991 *Chem. Phys. Lett.* **185** 23–30

[128] Weiss P S and Eigler D M 1993 *Phys. Rev. Lett.* **71** 3139–42

[129] Sautet P and Bocquet M L 1994 *Surf. Sci.* **304** L445–L50

[130] Futaba D N, Landry J P, Loui A and Chiang S 2001 *J. Vac. Sci. Technol.* A **19** 1993–5

[131] Futaba D N, Landry J P, Loui A and Chiang S 2002 *Phys. Rev.* B **65** 045106

[132] Loui A and Chiang S 2004 *Appl. Surf. Sci.* **237** 559–64

[133] Caldwell T E, Abdelrehim I M and Land D P 1996 *J. Am. Chem. Soc.* **118** 907–8

[134] Loui A 2005 *PhD Dissertation* Physics, University of California, Davis, CA

[135] Loui A, Futaba D N and Chiang S 2011 submitted

[136] Loui A, Fong C Y and Chiang S 2011 submitted

[137] Knight M J, Allegretti F, Kroger E A, Polcik M, Lamont C L A and Woodruff D P 2008 *Surf. Sci.* **602** 2524–31

[138] Knight M J, Allegretti F, Kroger E A, Polcik M, Lamont C L A and Woodruff D P 2008 *Surf. Sci.* **602** 2743–51

[139] Bradley M K, Robinson J and Woodruff D P 2010 *Surf. Sci.* **604** 920–5

[140] Bradley M K, Duncan D A, Robinson J and Woodruff D P 2011 *Phys. Chem. Chem. Phys.* **13** 7975–84

[141] Mate C M, McClelland G M, Erlandsson R and Chiang S 1987 *Phys. Rev. Lett.* **59** 1942–5

[142] Erlandsson R, Hadziioannou G, Mate C M, Mcclelland G M and Chiang S 1988 *J. Chem. Phys.* **89** 5190–3

[143] Mate C M, Erlandsson R, McClelland G M and Chiang S 1989 *Surf. Sci.* **208** 473–86

[144] Mamin H J, Ganz E, Abraham D W, Thomson R E and Clarke J 1986 *Phys. Rev.* B **34** 9015–8

[145] Soler J M, Baro A M, Garcia N and Rohrer H 1986 *Phys. Rev. Lett.* **57** 444–7

[146] Morita S, Tsukada S and Mikoshiba N 1987 *Japan. J. Appl. Phys. Part 2—Lett.* **26** L1511–L3

[147] Pethica J B 1986 *Phys. Rev. Lett.* **57** 3235